Interaction of urban heating and local winds during the calm intermonsoon seasons in the tropics.

OOI, M.C.G., CHAN, A., SUBRAMANIAM, K., MORRIS, K.I. and OOZEER, M.Y.

2017

AGU PUBLICATIONS

JGR

Journal of Geophysical Research: Atmospheres

RESEARCH ARTICLE
10.1002/2017JD026690

Key Points:
- The urban heating profile is greatly driven by cloud cover, atmospheric moisture content, and differential cooling rate
- The presence of urban significantly alters the onset and strength of topographic-induced flow in the coastal metropolitan
- Sea-and-valley-breeze-orientated synoptic flow shows great influences on the interaction of urban and topographic-induced flow

Correspondence to:
M. C. G. Ooi,
chelgee.ooi@gmail.com

Citation:
Ooi, M. C. G., Chan, A., Subramaniam, K., Morris, K. I., & Oozeer, M. Y. (2017). Interaction of urban heating and local winds during the calm intermonsoon seasons in the tropics. *Journal of Geophysical Research: Atmospheres*, *122*, 11,499–11,523. https://doi.org/10.1002/2017JD026690

Received 21 FEB 2017
Accepted 30 SEP 2017
Accepted article online 6 OCT 2017
Published online 7 NOV 2017

Interaction of Urban Heating and Local Winds During the Calm Intermonsoon Seasons in the Tropics

M. C. G. Ooi[1], A. Chan[1], K. Subramaniam[2], K. I. Morris[1,3,4], and M. Y. Oozeer[1]

[1]Division of Environment, Faculty of Engineering, University of Nottingham Malaysia Campus, Semenyih, Malaysia, [2]Climate and Weather Model Development Section, Malaysian Meteorological Department, Petaling Jaya, Malaysia, [3]Center of Excellence for Sustainable Innovation and Research Initiative, Port Harcourt, Nigeria, [4]Department of Mechanical Engineering, Ashesi University College, Berekuso, Ghana

Abstract Rapid urbanization of cities has greatly modified the thermal and dynamic profile in the urban boundary layer. This paper attempts to study the interaction of urban heating and the local topographic-induced flow circulation for a tropical coastal city, Greater Kuala Lumpur, in Malaysia. The role of sea-and-valley-breeze-orientated synoptic flow (SBOS) on the interaction is determined by comparing two intermonsoon periods. A state-of-the-art numerical model, Advanced Research Weather Research and Forecasting model, is used to identify the influence of urbanization through modification of urban surfaces. The model reasonably reproduces the vertical sounding data and near-surface weather parameters. The diurnal urban heating pattern is attributed to three predominant factors: (i) weak under calm and clear-sky condition (morning heating), (ii) weak under larger atmospheric moisture content (late afternoon convection), and (iii) largest (1.4°C) due to differential cooling rate of urban and rural surface at night. The interaction of urban thermals and upper level SBOS affects the effect of urbanization on local circulation during the day. The urban thermals reduce the weak opposing SBOS (<2 m s^{-1}) and enhance the inflow of moisture-rich sea breeze passage. This increases the intensity of downwind convective precipitation during late afternoon. On contrary, the strong opposing SBOS (>2 m s^{-1}) suppresses the vertical lifting of urban thermals and decelerates the sea breeze front. It is discovered that the interaction of urban heating and topographic-induced flow is interdependent while the synoptic flow plays a critical role in modifying both factors, respectively.

1. Introduction

The urban boundary layer (UBL) is the internal boundary layer above a city/urban region. It is formed in response to the buoyant, convective, and drag fluxes induced by the geophysical features and energy budget of the urban land surface (Oke, 1976; Stull, 1988). In contrast to the rural areas, the dynamic UBL is significantly hotter, drier, and more polluted (Barlow, 2014; Collier, 2006; Zhang, Zhu, & Zhu, 2011). Urban surfaces with high thermal inertia in addition to anthropogenic heat emission retain intense heat within narrow urban canyons and enhance the turbulent instability within the boundary layer, especially after sunset (Giovannini et al., 2013; Miao et al., 2009; Oke, 1995). The pressure depression induced by urban heat island (UHI) draws surrounding air toward the urban core, thereby creating the urban breeze with a diverged risen flow near the top of the UBL (Miao et al., 2009). The interactions of strong urban thermals with the natural topographic flow are analogously observed in inland and coastal cities (Freitas et al., 2006; Li et al., 2016; Miao et al., 2009; Ryu & Baik, 2013). As a result, the displacement or weakening/strengthening of these flows has significantly altered the rainfall patterns (Dixon & Mote, 2003; Kusaka et al., 2014; Thielen et al., 2000) and pollutant level within and around the city (Ji, Lee, & Lee, 2013; Thompson, Holt, & Pullen, 2007). The influence of urban thermals is further extended and complicated by the near proximity of urban to mountains and water body (Von Glasow et al., 2013).

The differential heating rate of land surface and sea creates the thermal gradient between the surfaces and induces sea (land) breeze during the day (night). Urbanization has two contrasting influences on the sea breeze flow propagation toward the urban cities. Increases in urban surface roughness enhance surface friction and drag that can decelerate atmospheric flow over coastal urban surface. The horizontal wind shear and frontal lifting due to surface roughness will delay the arrival of sea breeze front in the urban core. This is observed in cities including New York (Thompson et al., 2007), Greater Beijing (Zhong & Yang, 2015), and Toulouse (Hidalgo, Pigeon, & Masson, 2008). Such dynamical effect is also observed in Tian Jin (Miao et al.,

2015), Athens (Dandou, Tombrou, & Nikolaos, 2009), and Houston (Chen et al., 2011) but limited to the initiation stage of sea (land) breeze flow in the morning (evening) near the upwind of coastal region (urban core). This occurs when the differential heating of urban is less significant. Therefore, as soon as the thermal gradient between the urban and water is established to counter the dynamical drag, the sea breeze passage starts to accelerate toward the urban heat center in the noon. The strength of the sea breeze advection is subjected to the size of the city which induces UHI effect (Kang et al., 2014). Near the urban core, the combined vertical lifting and surface friction of urban thermodynamics forcing have caused the stagnation of sea breeze at the urban center before continue to push inland (Chen et al., 2011; Freitas et al., 2006; Ryu & Baik, 2013).

Studies have also found the influence of sea breeze passage on the urban heat circulation. Strong sea breeze has weakened the urban thermal and displaces the UHI around 5 km to 10 km downwind of the city, especially in cities located in close proximity to the water body (Dandou et al., 2009; Gedzelman et al., 2003). The UHI returns to the urban center following the dissipation of sea breeze at night (Chemel & Sokhi, 2012). The delicate balance of the sea breeze-urban breeze system is also subjected to the synoptic level condition. The strong prevailing synoptic condition has a suppressive effect on the urban heat circulation (Lemonsu & Masson, 2002; Seasman et al., 1988). However, the influence of synoptic condition on the topographic flow is directional; the landward synoptic flow enhances the sea breeze during the day (Gedzelman et al., 2003; Lai & Cheng, 2009). Conversely, when synoptic flow prevails in the opposite direction of sea breeze, sea breeze front developed is more prone to the accumulation of secondary pollutant in the rear of the front.

For cities bounded by elevated surfaces or features, the orographic movements such as up-, down- and cross-valley flows complicate the sea breeze-urban breeze circulation system. During the daytime, the air from the valley blows uphill and weakens the urban breeze on the hillside from the opposite direction (Miao et al., 2015; Ryu & Baik, 2013). The valley breeze has enhanced the sea breeze passage, unlike the flat plain region that stagnate the sea breeze before the urbanized agglomeration (Ohashi & Kida, 2002). However, the UHI tends to suppress the night inversion which weakens the down-valley flow and prolongs the duration of lake/sea breeze periods (Giovannini et al., 2013; Miao et al., 2015). It is also found that a city located within a valley region with a crossing water body is more prone to pollutant accumulation due to recirculation of air back to the land as observed in the Pearl River Delta and the Straits of Malacca (Fujita, Kimura, & Yoshizaki, 2010; Lo et al., 2006).

Sitting at the heart of Maritime Continent (MC), weather prediction of Greater Kuala Lumpur (GKL), Malaysia, is trickier due to the heterogeneity of land-sea mask. The large composition of water body within the scattered land surface complicates the weather and hydrological cycle in the region (Chang et al., 2005; Kikuchi & Wang, 2008). Among all western coastal states of Peninsula Malaysia, the case study region, GKL, is well shaded by the central backbone of the peninsula, Titiwangsa mountain range, and the Sumatra island (Oki & Musiake, 1994; Varikoden, Samah, & Babu, 2010). The geographical location produces a contrasting precipitation profile in the region of GKL and highlights the individuality of local weather. The orientation of coast being perpendicular to the prevailing monsoonal wind causes such an out-of-phase climatic behavior more pronounced among the rest of the MC region (Ding & Chan, 2005). In the case of GKL, the sea (land) breeze orientates with the valley (mountain) breeze for the narrow plain between coastline and higher terrain. Therefore, the local flows including land-sea and orographic flow are prone to change due to the presence of GKL along the path. Despite the complexity of the MC region, studies on urban boundary layer in the Southeast Asia are still lacking compared to other tropical and subtropical regions (Roth, 2007).

The urban region is able to induce local circulation and also modifies the topographic flow as demonstrated in the previous studies. To resolve the movement of current, a high-resolution numerical simulation tool, the Advanced Research core of the Weather Research and Forecasting (WRF-ARW) system version (v3.6.1), is used (Wang et al., 2015). This paper aims to investigate the effect of urbanization on the regional boundary climate in GKL, with particular interest in its interaction with the evolution of land-sea and orographic flow. Investigations are also conducted during two intermonsoon periods to evaluate the implications of synoptic flow on the interaction of the urban and topographic-induced circulation. To ensure the appropriate representation of boundary layer, the model is tested against the measurement and sounding data in the

Table 1
Weather Information Extracted From the Measuring Stations Marked in Figure 3, Except for the Rain Data Which are Extracted from Sepang (ST6) Only

Weather parameters		October	April
Temperature (°C)	Daily	27.1	27.5
	Daytime (0830–1730)	29.6	30.6
Humidity (%)	Daily	77.1	81.1
	Daytime (0830–1730)	66.9	69.1
Wind speed (m s^{-1})	Daily	1.5	1.2
	Daytime (0830–1730)	2.1	1.7
Precipitation recorded at ST6*	Total rain amount (mm)	42.8	324.6
	Rain (total) percentage throughout the day	9.6%	15.7%
	Occurrence of rain (total) from 2100 to 0800 MYT	49%	15%
	Rain (thunderstorm) percentage throughout the day	4.1%	11.8%
	Occurrence of rain (thunderstorm) from 1400 to 2000 MYT	21%	55%

Note. Data are compiled during the 18 day simulation period. MYT stands for Malaysian Time.

area to assess the strengths and weaknesses before applied to the UBL study in the most developed metropolitan in Malaysia.

2. Model Settings

2.1. Background Weather

The climatic forcing from mainland Asia plays an immense role on the seasonal wind field and precipitation pattern in Malay Peninsula (Sani, 1977). The North-East Monsoon during boreal winter (November to March) carries large amount of moisture to the Malay Peninsula. The South-West Monsoon (SWM) during boreal summer (May to September) carries dry air to the Malay Peninsula after rain shadowed by Sumatra island. The SWM is the active biomass burning season when the atmospheric aerosol quality, cloud formation, and radiation amount are altered substantially in Southeast Asia (Lin et al., 2013; Reid et al., 2013). Formation of the complete urban heat circulation is intense during the weak synoptic period under a clear-sky and calm condition (Lai & Cheng, 2009; Santamouris, 2015). Hence, considering on the study of local weather phenomenon, periods with less seasonal synoptic atmospheric forcing and rainfall anomalies are preferred (Jauregui, Godinez, & Cruz, 1992; Santamouris, 2015). The two calm intermonsoon months, April and October, with minimal seasonal convection on local weather of west coast of Malaysia are chosen to represent the boreal spring and boreal fall, respectively (Li et al., 2013; Sani, 1977). Under El-Niño (La-Niña) period, Southeast Asia experiences above (below) average sea surface temperature and receives lesser (more) rainfall and variation in atmospheric composition (Inness et al., 2015; Tangang & Juneng, 2004). Although there is no established study that suggest the role of El Niño–Southern Oscillation (ENSO) on the urban heat, potential variability of the heat and precipitation induced by the precipitation anomaly might confuse with urban-heat signal (Tangang et al., 2012). Therefore, the period of intense ENSO as well as severe haze episode is screened out (Department of Environment Malaysia, 2016; NOAA, 2017), and the current urban study focuses in 2003, the year of weak El-Niño (McPhaden, 2004). According to the measurement from the eight weather stations in GKL (white markers in Figure 3), the region receives rather weak winds with average wind speed of 1.7 m s^{-1} and 2.1 m s^{-1} in April and October, respectively. The weather data compiled in Table 1 shows that April experiences higher average daytime temperature of 30.6°C and a higher amount of precipitation, compared to October (29.6°C). Convective raining usually occurs during the late afternoon in the April and nighttime in October (Oki & Musiake, 1994). Such diurnal rainfall signal is common in the MC due to the presence of mountain near the coastline in the region (Bhatt, Sobolowski, & Higuchi, 2016; Sow et al., 2011; Teo et al., 2011).

On the mesoscale profile shown in Figure 1, strong synoptic wind is observed in October blowing toward the southeast direction while April is experiencing weaker winds from northeast. Similar to the rain gauge result, spatial profiles in Figures 1a and 1b show more precipitation activities over GKL during April compared to October month. A contrasting precipitation profile is observed at the Straits of Malacca off the coast of GKL rest of MC in Figures 1a and 1b. Following the withdrawal of the winter monsoon in April, the

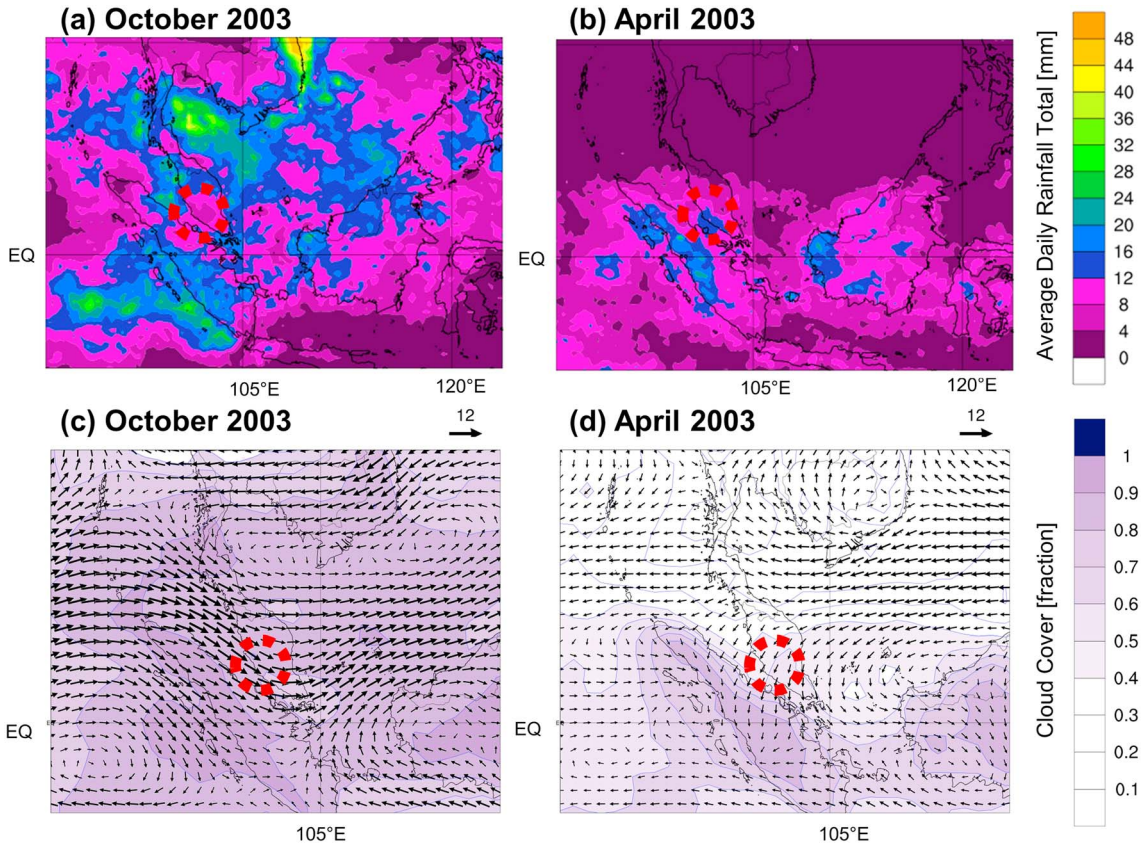

Figure 1. Precipitation profile extracted from Tropical Rainfall Measuring Mission (TRMM) for (a) October and (b) April. The TRMM data set uses the daily accumulated precipitation product at level 3 (3B42) generated from the 3-hourly research quality derived with the version 7 TRMM Multi-Satellite Precipitation Analysis (TMPA) algorithm. The figure shows the daily-averaged product during the period of study (refer to section 2.2). Cloud cover profile and wind field at 850 hPa from the ERA-interim reanalysis data (Dee et al., 2011) for (c) October and (d) April. Location of GKL is marked with red dotted circle. EQ stands for equator.

weakening of prevailing anticyclone, if any, over the Bay of Bengal significantly reduces the strength of north easterlies over east coast of Malay Peninsula (Ding & Chan, 2005). The sea breezes from the Straits of Malacca and north easterlies originating from the east coast enhances the convergence over the GKL in April (Joseph et al., 2008). On the other hand, the asymmetrical movement of monsoon trough from the boreal summer to winter forms a low-pressure belt off the coast of Borneo in October (Chang et al., 2005). The pressure depression converges the westerlies from equatorial Indian Ocean to flow past the Malay Peninsula as shown in Figures 1c and 1d. It carries a large amount of moisture over the MC region well before the onset of the winter monsoon in 2003 (Moten et al., 2014). The mountain ridge on the Sumatra island subsequently obstructs the moisture bearing flow and creates a wet and cloudy environment for the entire MC but it is particularly dry in GKL in October.

2.2. Model Physics and Experiment Design

All simulations are initiated from 0800 Malaysia Time (MYT) starting on first day to 0800 MYT of twentieth day for April and October in 2003. The simulation periods selected fall well within the transitional period of the two monsoon seasons (Diong et al., 2015; Moten et al., 2014). The analyzed result excludes the first 24 h which is used as a spin-up period for steady throughput. The remaining 18 days are then used for analysis throughout in this paper. The parent domain covering the entire Malaysia (including Borneo) is dynamically downscaled from 27 km to 9 km, 3 km, and 1 km to the Selangor state (d04) as shown in Figure 2. Here 37 vertical eta levels were used with model's top at 50 hPa. Fifteen of the lowest vertical layers are reserved below the lowest 2 km of boundary layer to further resolve rapid atmospheric changes. The initial and lateral boundary conditions are obtained from the 6-hourly ERA-Interim Reanalysis data processed by European Centre for Medium-Range Weather Forecasts (Dee et al., 2011). The simulation updates the original

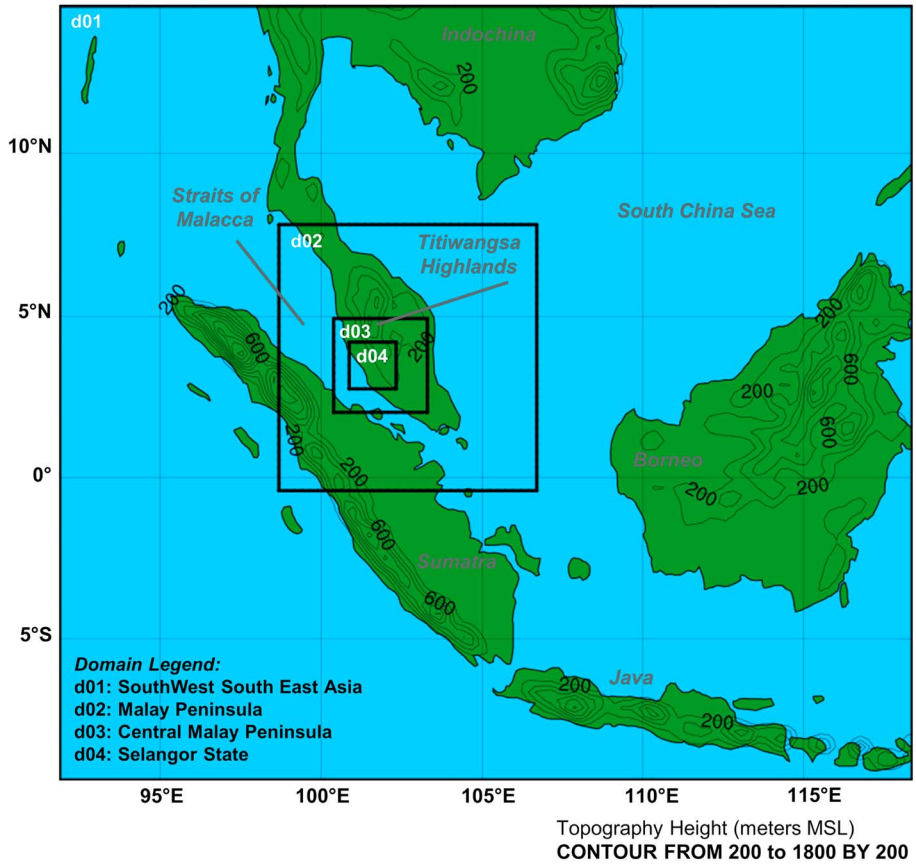

Figure 2. Domain settings and location map with terrain height information for WRF simulation; d is denoted as domain with the following numbering indicates the number of domain.

Moderate Resolution Imaging Spectroradiometer land use map to incorporate three urban subdivisions and better represent the built-up area as shown in Figure 3. Single-layer urban canopy model (UCM) package with detailed specification urban morphology is coupled with Noah Land Surface Model to bridge the gap between microscale urban land surface environment and near-surface layer atmospheric conditions (Chen et al., 2011). It is shown that the locally calibrated urban parameters, including impervious portion of urban grid, canopy geometry, and thermal properties, have substantially improved the prediction of the near-surface temperature and wind field (Morris et al., 2017; Ooi et al., 2017). The atmospheric heating fueled by longwave and shortwave radiation budget is resolved through the Rapid Radiative Transfer Model (Mlawer et al., 1997).

The local planetary boundary layer (PBL) scheme, Mellor-Yamada-Janjić (MYJ), is able to predict the generation, transportation, and dissipation of turbulent kinetic energy and the entrainment near PBL top (Janjic, 1994; Skamarock et al., 2008). Preliminary comparative study found that the MYJ shows an edge to reproduce the stable and localized boundary layers during the monsoon transitional period compared to the nonlocal PBL schemes, Yonsei University and Asymmetrical Convective Mechanism. In WRF, the MYJ PBL scheme is tied to Janjić Eta Monin-Obukhov (Eta) surface layer scheme. The latter is adjusted to parameterize the thermal roughness length according to land use (MZT) to improve the heat exchange processes between atmospheric and ground vegetation (Chen & Zhang, 2009). It outperforms the MM5 surface layer scheme bonded to the nonlocal PBL schemes and predicts a closer approximation of near-surface temperature, water mixing ratio, and rainfall amount. The heterogeneous land sea mask in MC shelters the GKL region from large-scale turbulence movement and creates a relatively calm weather condition compared to the rest of the Malay Peninsula (Chang et al., 2005). In such a context, the local scheme (MYJ) remains a more suitable candidate of PBL scheme for the current study under relative stable weather condition, resonating with the findings from Shin and Hong (2011).

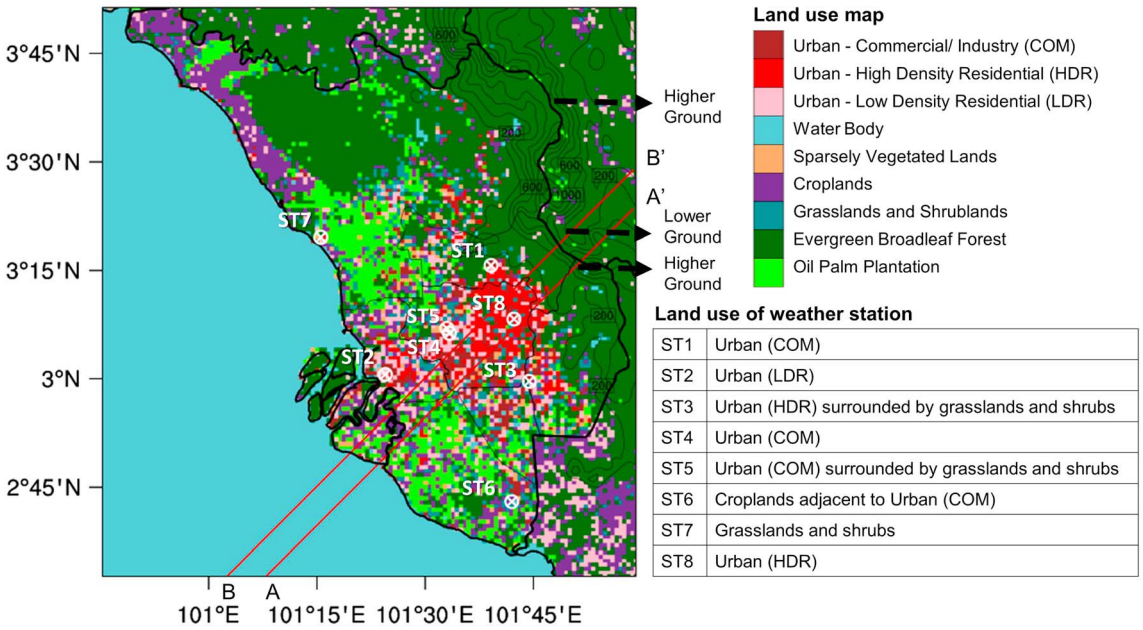

Figure 3. Existing land use map (URB) with terrain height (contour). Two lines have indicated the vertical cross-sectional profile extracted in later analysis. AA′ has crossed plane (70,28) while BB′ crosses plane (60,28), both with angle of 45°. ST1 to ST8 are stations where near-surface measurement data is extracted. ST6 (Sepang) also provides the sounding data.

The model is found to produce greater error during the days with heavy precipitation. In order to reduce the model uncertainty stemmed from single physics representation, this paper incorporates the multiphysics ensemble study for cumulus and microphysics schemes (Berner et al., 2011; Toth, 2001). The physics options incorporated include Betts-Miller-Janjić (BMJ) and Kain-Fristch (KF) cumulus schemes, as well as Purdue Lin single moment (Lin) and WRF Single-Moment 6-Class (WSM6) microphysics schemes. The moisture cycle is explicitly parameterized with the two microphysics scheme to determine the mixing ratios of water substance in six forms including water vapor, cloud water, rain, ice, snow, and graupel. They adopted the similar graupel processes (Lin, Farley, & Orville, 1983) but WSM6 scheme improves rainfall prediction by introducing separate saturation process for ice and water and the sedimentation/accretion process for snow and graupel (Hong, Dudhia, & Chen, 2004; Hong & Lim, 2006). Both schemes are suitable for high-resolution research purpose in tropical study (Cruz & Narisma, 2016; Skamarock et al., 2008). The cumulus scheme is incorporated for the two outer domains (grid scale larger than 5 km) where the aforementioned microphysics routine is unable to resolve the horizontal and vertical subgrid-scale fluxes of the cloud (Janjic, 1994). The statistical-equilibrium scheme, BMJ scheme, has reproduced the convective rainfall pattern and intensity well (Salimun, Tangang, & Juneng, 2010) in the Malay Peninsula where the afternoon precipitation mainly occurs due to instability of rising air movement over mountain (Sow et al., 2011; Teo et al., 2011). The KF convective scheme that releases the instability capped from convective inhibition has reproduced the diurnal precipitation cycle in the MC (Bhatt et al., 2016). The combination of WSM6 microphysics and KF convective is omitted due to the instability generated and overly estimated vertical wind speed that diverges up the boundary layer. Hence, the three ensemble members adopted for this study that represent the microphysics and cumulus schemes, respectively, are (a) Lin and BMJ, (2) WSM6 and BMJ (2), and (3) Lin and KF.

Simulation cases are respectively run for the two aforementioned intermonsoonal periods to evaluate their corresponding performance with cases set up. With bilinear interpolation of neighboring grids, all cases are verified against near-surface measurement data obtained from eight weather stations while vertical sounding profile is limited to Sepang station (ST6) operated by Malaysia Meteorological Department (MMD) and Department of Environment (DOE) as shown in Figure 3. Knowing the low reliability of the measured wind direction under calm winds, the verification wind direction data with wind speed weaker than 1.5 m s^{-1} is filtered out (Zhang, Pu, & Zhang, 2013). The no urbanization case (noURB) is run with the similar ensemble model settings but replaces the urban land use with the surrounding vegetated surfaces. The

fictitious case is designed to indicate the influence of urban presence on boundary climate compared to its surrounding land use while isolating the spatial variation of background climate. The grassland and shrubs land use category with larger sky view factor is also chosen as the nonurban surface due to the great contrast of thermal response compared to the urban surfaces (Li et al., 2013). The approach is widely applied to identify the sole impact of urbanization in the urban climate sector (Freitas et al., 2006; Thompson et al., 2007).

3. Model Evaluation

3.1. Vertical Profile

The performances of the model in October and April are evaluated with available sounding data during the morning and night transitional hours at 0800 MYT and 2000 MYT. The major difference between the two intermonsoon periods is shown in the vertical wind profile. Strong northwest winds dominate the upper layer atmosphere in October as illustrated in Figures 4c and 4d while April experiences weak influence of northeasterlies as shown in Figures 4g and 4h. The former agrees well with the reanalysis data at 850 hPa level portrayed in Figures 1c and 1d. In October, the prevailing flow driven by the convergence belt near Borneo (Chang et al., 2005) is flowing from northwest with wind speed up to 9 m s^{-1} in the range of 1000 m to 1400 m height throughout the day (Figure 4c) where the convective heating in the Asian monsoon region is most indicative (Wang, Wu, & Lau, 2001). The strong shearing at this level therefore implies that intensive convective heating and moisture convergence are occurring over the boundary layer. All simulated cases typically generate a weaker jet flow at higher height. The underestimation of horizontal wind speed from 800 m to 1600 m is mainly stemmed from the low-level jet (centered at 1000 m) develops from 4 to 8 October 2003. It is a potential result of enhanced mixing produced by MYJ PBL scheme, though the local PBL scheme generates more localized mixing compared to the nonlocal counterparts (Balzarini et al., 2014; Xie et al., 2012). Similar findings suggested that the discrimination remains the systematic error of unrealistic of PBL parameterization that prone to enhanced vertical mixing (Storm & Basu, 2010; Zhang et al., 2013). Despite the weaker intensity of the low-level jet, the model has reasonably captured the period of occurrence. The weak low-level jet on the layer in Figure 4c hence induces the cold (Figure 4a) and wet bias (Figure 4b) in October.

In April, the vertical wind profile shows a smoothly increasing curve with a slight inflection near the stable boundary layer in Figures 4g and 4h. Similarly, the boundary layer winds below 500 m flows from the north around 2000 MYT while the simulation result shows an inclination to the northwest but returns to north around 2200 MYT. The interaction of land surface and atmospheric level is imperative under frontal condition in April especially the coupling performance of surface layer parameterization (Pichelli et al., 2014; Zhang et al., 2013). The model performance is tabulated in Table 2 and is evaluated with mean absolute error (MAE), root-mean-square error (RMSE), and fractional average error (FAE),

$$\mathrm{MAE} = \frac{1}{\boldsymbol{Nt}} \sum |\boldsymbol{M_{ni}} - \boldsymbol{O_{ni}}| \tag{1}$$

$$\mathrm{RMSE} = \left(\frac{1}{\boldsymbol{Nt}} \sum (\boldsymbol{M_{ni}} - \boldsymbol{O_{ni}})^2 \right)^{1/2} \tag{2}$$

$$\mathrm{FAE} = \frac{1}{\boldsymbol{Nt}} \sum \frac{|\boldsymbol{M_{ni}} - \boldsymbol{O_{ni}}|}{(\boldsymbol{M_{ni}} + \boldsymbol{O_{ni}})/2} \tag{3}$$

where n is the station number, i is the simulation time in hour, N is the total number of stations, and t represents the total simulation hours. M and O represents the modeled and observed variables, respectively. On the vertical scale, it shows an overall better accuracy during April than October during the transitional phase of boundary layer. The local parameterization scheme (MYJ) is known to estimate vertical quantities through prognostic eddy diffusivity of adjacent grids and hence simulate cases under stable and slightly unstable condition better compared to convective condition (Mellor & Yamada, 1982). Despite the stronger vertical mixing during the low-level jet in October, it has an edge in solving stable and localized boundary conditions in the calm month of April. Up to this point, the model is only verified when the sounding is available during the stability transitional phase. Therefore, it is only representative during the entraining and detraining process between the stable and unstable atmospheric condition when the model is evaluated. The temporal verification is subsequently complemented with the diurnal evaluation of the near-surface weather parameters.

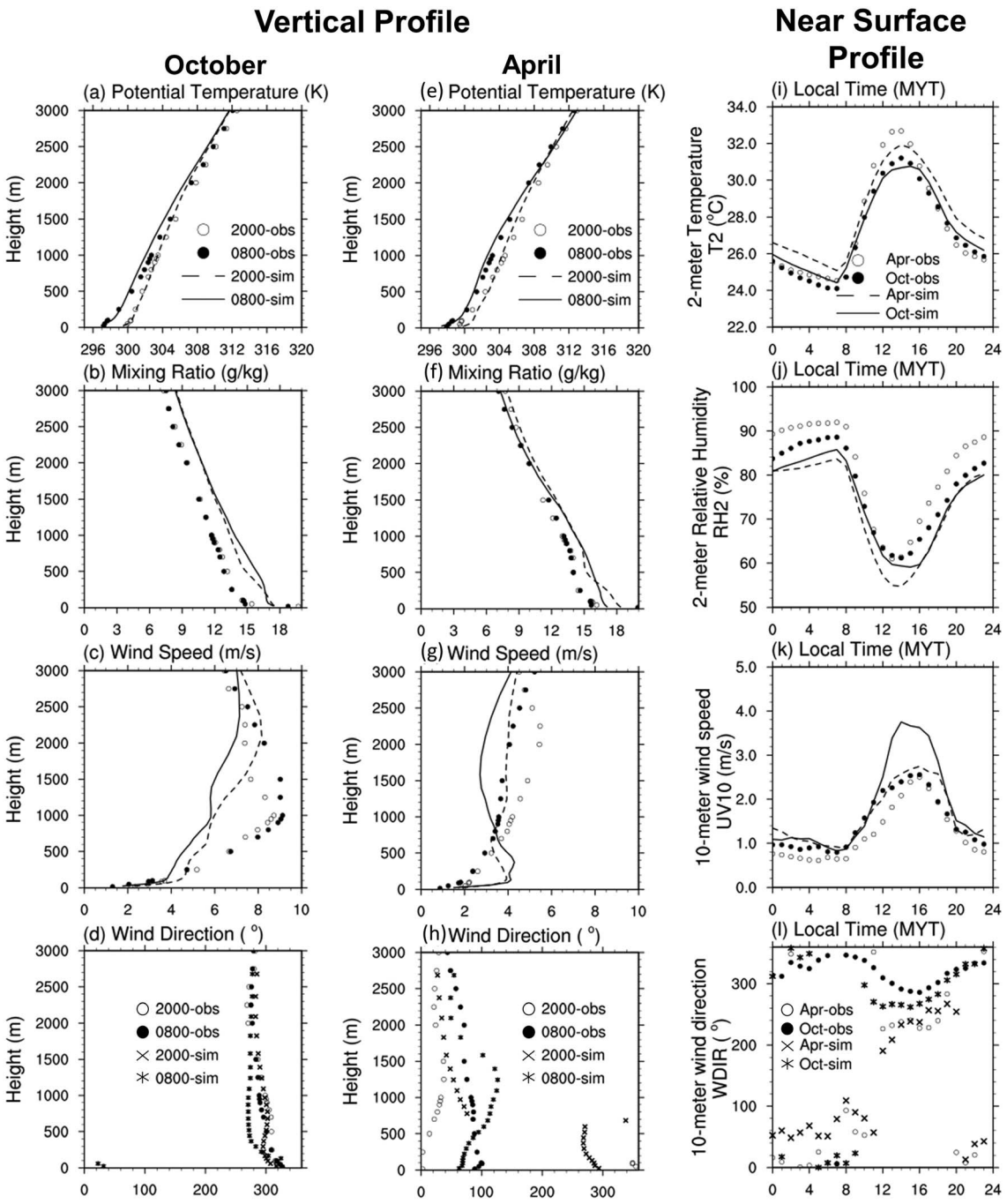

Figure 4. Evaluation of model performance to sounding data (in markers) for vertical profile of (a and e) potential temperature, (b and f) mixing ratio, (c and g) wind speed, and (d and h) wind direction against sounding data at 0800 MYT and 2000 MYT in October (column 1) and April 2003 (column 2), respectively. Hourly averaged of (i) 2 m air temperature, (j) 2 m relative humidity, (k) 10 m wind speed, and (l) 10 m wind direction extracted for grid points that collocate with eight ground observation stations in October and April 2003 (column 3).

3.2. Near-Surface Characteristics

Diurnal data from ground weather network are compiled to examine the performance of accompanying surface layer scheme of each PBL scheme that resolves the exchange of surface heat (Shin & Hong, 2011). The near-surface condition of simulation result is averaged over the study period to produce the hourly variation profile. In Figure 4i, the model reproduces the hourly 2 m temperature (T2) trend reasonably well with a cold bias attained for peak temperature at 1400 MYT in April. A generally lower amplitude variation is observed;

Table 2
Diurnal Analysis Error Indices for Model Performance in Vertical and Near Surface Parameters

Month	October		April		October		April		October		April	
Vertical	Temperature (°C)				Mixing ratio (g/kg)				Wind speed (m/s)			
Time	0800	2000	0800	2000	0800	2000	0800	2000	0800	2000	0800	2000
MAE	0.43	0.38	0.33	0.18	1.53	1.42	1.09	1.39	1.38	1.06	0.90	0.79
RMSE	0.50	0.49	0.37	0.24	1.75	1.56	1.28	1.77	1.81	1.31	1.07	0.91
FAE[a,b]	0.14	0.12	0.11	0.06	0.13	0.13	0.10	0.10	0.22	0.17	0.27	0.21
Near surface	2 m temperature (°C)				2 m relative humidity (%)				10 m wind speed (m/s)			
Average OBS	27.09		27.49		77.08		81.12		1.47		1.22	
MAE	1.31		1.65		6.74		9.62		0.92		0.83	
RMSE	1.65		2.08		8.56		11.67		1.26		1.15	
FAE[a]	0.05		0.06		0.09		0.13		0.62		0.65	
R2[a]	0.67		0.64		0.58		0.65		0.31		0.26	
NMAE[a]	0.05		0.06		0.09		0.12		0.63		0.69	

[a]FAE, R2, and NMAE are dimensionless. [b]The vertical potential temperature is multiplied by 100.

that is, modeled result is colder during the day and hotter at night, and is pertinent to the diurnal anthropogenic heat which is lacking in the current configuration of UCM (Lin et al., 2008; Morris et al., 2017). The air within the tropical wet region is humid all year round (Roth, 2007), with no less than 60% relative humidity. Figure 4j shows results for the 2 m relative humidity derived from the water vapor mixing ratio. In contrast with the vertical level, the scheme underestimates the humidity level during April but good agreement is attained in October during the day.

In comparison with the discussed surface variables, it is notable that the wind profile shows less diurnal variation over the two months. The model captures the diurnal variation of 10 m wind speed and produces stronger airflow during the day, in response to the perturbative movement induced by the heated land surface as shown in Figure 4k. Resonating with other WRF case studies conducted within flat plain valley region, the near-surface wind strength is generally overestimated throughout the day (Jiménez et al., 2013; Pichelli et al., 2014; Xie et al., 2012). It is discovered that the stronger wind is a result of underestimated surface drag of WRF model that only resolves the vegetation roughness (Mass & Ovens, 2011). The inclusion of orographic factor into the subgrid-scale surface drag parameterization is shown to reduce the positive error of 10 m wind speed. The scheme depends greatly on the topographic representation and initial condition of soil layers but is not available for the working PBL scheme (Jiménez & Dudhia, 2012; Wang et al., 2015). The 10 m wind direction is fairly predicted throughout the day with mean bias of 17° as shown in Figure 4l. Among which, the model captures the abrupt change of wind direction from northeast to southwest direction around 1000 to 1200 MYT in April. During these hours of sea breeze passage, the rapid shift of land to sea breeze in periods of weak synoptic influence has slightly affected the reproduction of 10 m wind direction which is more dependent to the surface conditions and land surface model (Cheng & Steenburgh, 2005; Zhang et al., 2013). Table 2 compiles the model performance to predict near-surface parameters using additional error indices, namely, the correlation coefficient (R^2) and normalized mean absolute error (NMAE),

$$\mathrm{NMAE} = \frac{\sum |\boldsymbol{M_{ni}} - \boldsymbol{O_{ni}}|}{\sum \boldsymbol{O_{ni}}} \tag{4}$$

The result shows satisfying agreement with the observation data, and performance is comparable among both months. The near-surface profile associates closely to the surface layer parameterization that resolves the exchange of the surface heat. This implies that the Eta similarity theory of MYJ scheme determines the 2 m temperature and relative humidity well. The good performance of the local scheme is also attributed to incorporation of modified surface layer approach. It resolves the heat transfer coefficient according to the roughness length of the surfaces and shown to improve especially the heat exchange processes between atmospheric and ground vegetation (Chen & Zhang, 2009). It also reliably addresses the entrainment effect on near-surface temperature during transition from stable boundary to convective layer. Initial surface condition and improvement to surface drag parameterization is capable to further improve the model predictability. However, at presence stage, considering the strong coupling of the MYJ PBL, Eta similarity surface

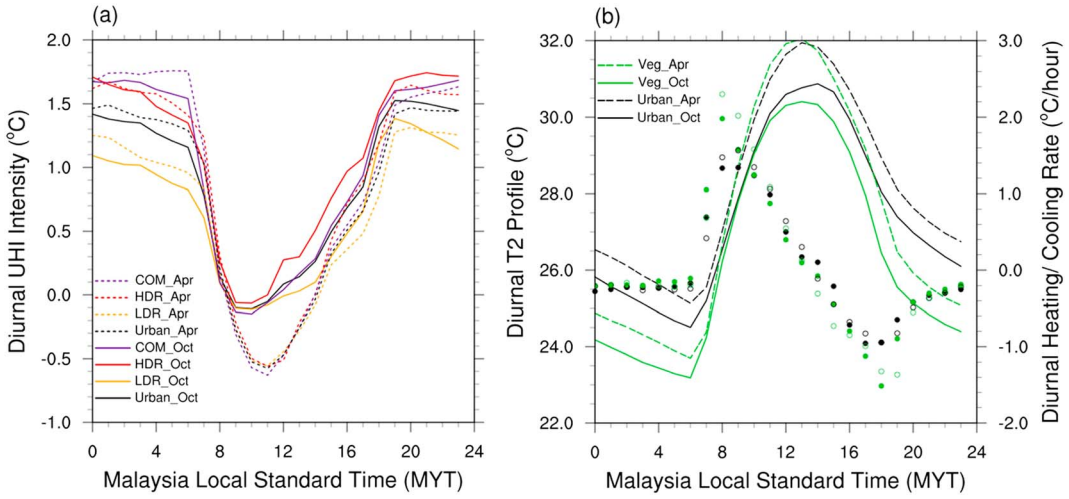

Figure 5. (a) Hourly averaged UHI intensity of urban surfaces (COM, HDR, LDR, and all urban) obtained through the difference between simulation and noURB case. (b) Diurnal T2 profile (line: October; dotted line: April) and heating/cooling rate (filled dot: October, hollow dot: April) in both April and October months for urban surface (urban) and after being replaced by vegetation (veg).

layer, and ensemble members of microphysics and cumulus schemes, it prompts the subsequent analysis on the effect of urbanization to be conducted with the combination.

4. Effect of Urbanization on Local Climate

4.1. Diurnal Analysis of Canopy Urban Heat Island (UHI) Intensity

The thermal response of canopy level to urbanization is indicated through the difference of diurnal 2 m temperature between the simulation case with and without urban development (noURB). The discrepancy is known as the UHI intensity. Figure 5a records daily-averaged UHI intensity of 0.88°C and 0.77°C for October and April, respectively. The intensity profile varies between three time segments: night (1900 to 0700 MYT), morning (0900 to 1300 MYT), and evening (1500 to 1800 MYT). The highest intensity profile of 1.35°C is observed for both months after sunset from 1900 to 0700 MYT. The vegetated surface cools down at a higher rate than the urban surface and subsequently increases the nocturnal UHI intensity as shown in Figure 5b. The urban surface cooling at night decreases from low-density to high-density residential and commercial regions characterized. The differential cooling is characterized with higher heat capacity, lower surface heat emissivity, and lower aspect ratio of urban canopy (Grossman-Clarke et al., 2008; Loughner et al., 2012; Oke & Maxwell, 1975). The positive UHI phenomenon agrees with the spatial distribution of temperature difference in Figure 6. The presences of the rough urban surface as well as the heated urban convergence zone impede the mountain flow and thus the outflow of the urban air mass (Li et al., 2013; Miao et al., 2015). Despite being the hotter month, the nocturnal UHI intensity in April remains comparable to October due to the reference rural region that is equally hot at night. This affirms that the nocturnal UHI effect is less governed by the temperature variation between the months.

The UHI intensity at the hottest period around 1400 MYT (Figure 5) approximates zero for both period of investigation. The minimal influence of urban during the peak temperature hour is equally shown in Singapore city which shares similar weather background (Li et al., 2013). During the morning heating period (0900 to 1300 MYT), April yields a strong negative intensity up to −0.58°C in Figure 5a. Such "cool pool" phenomenon is commonly observed in UHI study (e.g., Chow & Roth, 2003; Jauregui et al., 1992). Similar to the decelerated cooling at night, the urban surfaces experience a lower heating rate and thermal admittance due to the shadowing effect of tall buildings which hinders the absorption of radiative heat (Oke, 1987; Santamouris, 2015). In Figure 5b, the greater heating rate of vegetation in the morning of April highlights the immediate thermal response of the dry surface to the radiative cycle. As such, the humid vegetation cover caused by late night precipitation in October is heated up slower and therefore explains the near-zero UHI intensity (−0.01°C). The prolonged effect of regular heavy showers and thunderstorm on

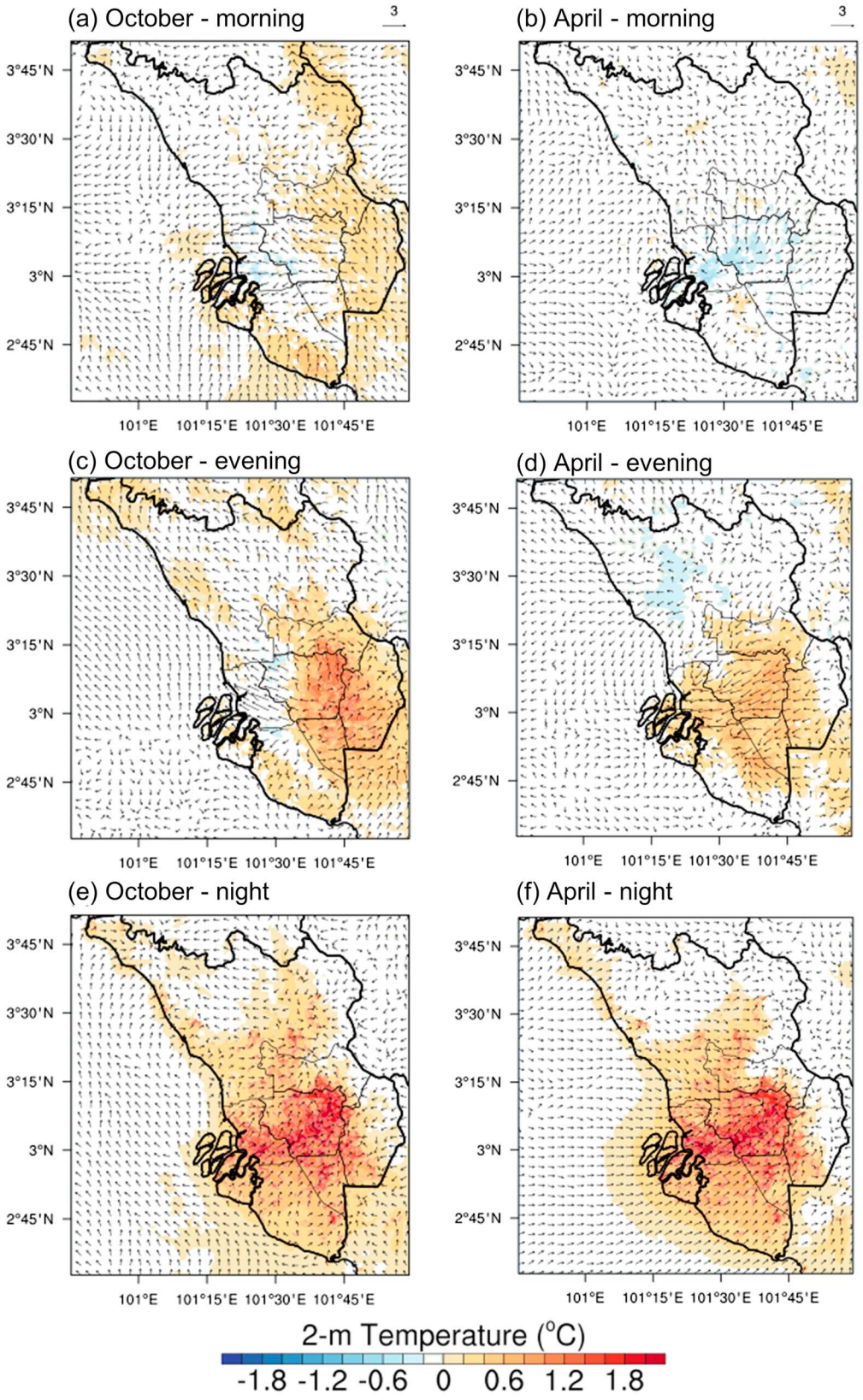

Figure 6. Spatial difference of 2 m temperature (°C) and 10 m wind vector (m/s) with noURB case at (a and b) morning, (c and d) evening, and (e and f) night for October (left column) and April (right column). The diagram has masked out less significant thermal difference between −0.1°C and 0.1°C.

the UHI intensity of the subsequent days is also pointed out by Kim and Baik (2002). This agrees well with the other low-latitude cities where the thermal response is predominantly governed by the wet/dry condition that than the hot/cold variation of the midlatitude cities (Arnfield, 2003; Jauregui, 1997). The clear sky in April facilitates the radiative heating transfer of the surface heat which the entire land surface heats up uniformly, as illustrated in Figures 8a and 8b and 7. It similarly enhances the radiative cooling of the heated surface as shown in Figure 6 which the cool pool is formed for the urban region. Inversely, The widespread coverage of cloud in (Figure 8) October inhibits the vertical transportation of near-surface air (Morris, Simmonds, & Plummer, 2001). It also decelerates the dissipation rate of heat generated at the urban and explains the accumulation of heat over the land mask as shown in Figure 6.

Subsequently, April yields UHI intensity of 0.61°C, 0.22°C lower than that of October from 1500 to 1800 MYT, when the afternoon convective precipitation occurs. The concurrence of precipitation activities suggests the association of the prevailing moisture-bearing sea breeze flow and the UHI intensity. The urban surface generates a clear profile of "urban dry island" with lower moisture content in Figure 8. The urban upwind region in October, in particular, forms a cool pool (Figure 6c) with higher moisture content compared to the adjacent urban (Figure 8c). The presence of urban land along the wind path reduces the strength of the sea breeze on the upwind side of the urban. This indicates that the strong inland urban heating draws immense moisture from the sea to the coastal region during the initiation hour of afternoon convective precipitation. The increment of precipitation tendency due to urbanization is highlighted in several cities (Daniels et al., 2016; Zhong & Yang, 2015). During this period, the urban heat is mutually affected by the interaction of sea breeze and synoptic weather condition which is further discussed in section 4.2. The urban cool pool recedes gradually and gives way to the growing urban heating patch in the evening. A prominent UHI is formed at night in both months (Figure 6).

In April, the sea breeze stalls on the upwind of the urban core in the evening period (Figure 6) due to the inflow of gap winds (lower ground marked in Figure 3) and its driven mountain breeze from the inland mountain range. Around evening period in Figure 7, the sea breeze sweeps past GKL and converges near the gap located on the right of the GKL (marked as lower ground in Figure 3) which acts as an aperture. The lower strength of UHII in April month is likely to be attributed to the reduction of sea breeze strength and hence the moisture inflow. The varied response of daytime UHI intensity highlights the potential tendency of daytime UHI to respond differently to the synoptic condition during the two intermonsoonal seasons. The interaction of UHI and local topographic flow is further elaborated in the subsequent section.

The synoptic effect imposes larger urban-induced thermal response during the day than the night of both transitional months in the tropical region. In the morning to midday, clear sky is responsible for the formation of urban cool pool in April. The enhanced sea breeze flow due to urban confluence zone has effectively subdued the urban heating effect on the upwind of urban in the evening. The passages of sea/land breezes and mountain/valley breezes vary according to the synoptic condition by comparing the two months. The presence of urban surface therefore alters the circulation of these flows depending on the synoptic frontal condition.

4.2. Sea-Land Breeze and Orographic Breeze Circulation

The vertical dynamics of local climatic circulation is investigated through the cross-sectional profile (AA′) that cut perpendicularly across the sea surface, urban, and the elevated ground on the east as illustrated in Figure 3. In this context, the influence of synoptic forcing (~850 hPa) on the local circulation is only accounted for the portion which is orientated to the sea/valley (land/mountain) breeze. Therefore, despite the strong synoptic forcing in October, the GKL region experiences weak synoptic flow which orientates with the sea breeze (SBOS) as seen in Figure 1b. Such condition is conducive for the formation of weak sea breeze front (SBF). Conversely, the weak synoptic condition (Figure 1b) in April is flowing on the direct opposite of the sea breeze flow on the 850 hPa level but not sufficiently strong to prevent the formation of sea breeze as discussed below. This thereby forms a strong SBF condition.

4.2.1. October

At 1300 MYT, the strength of the sea breeze is strengthened from 2.52 m s^{-1} (noURB) to 2.83 m s^{-1} by the confluence region created near the heated urban surface as shown in Figure 9. The stagnation of sea breeze that is equally found in noURB is accounted as the blocking effect of the elevated terrain (Qian, Epifanio, & Zhang, 2012). At 1500MYT, a large amount of moisture is carried into the upwind side of the urban as shown

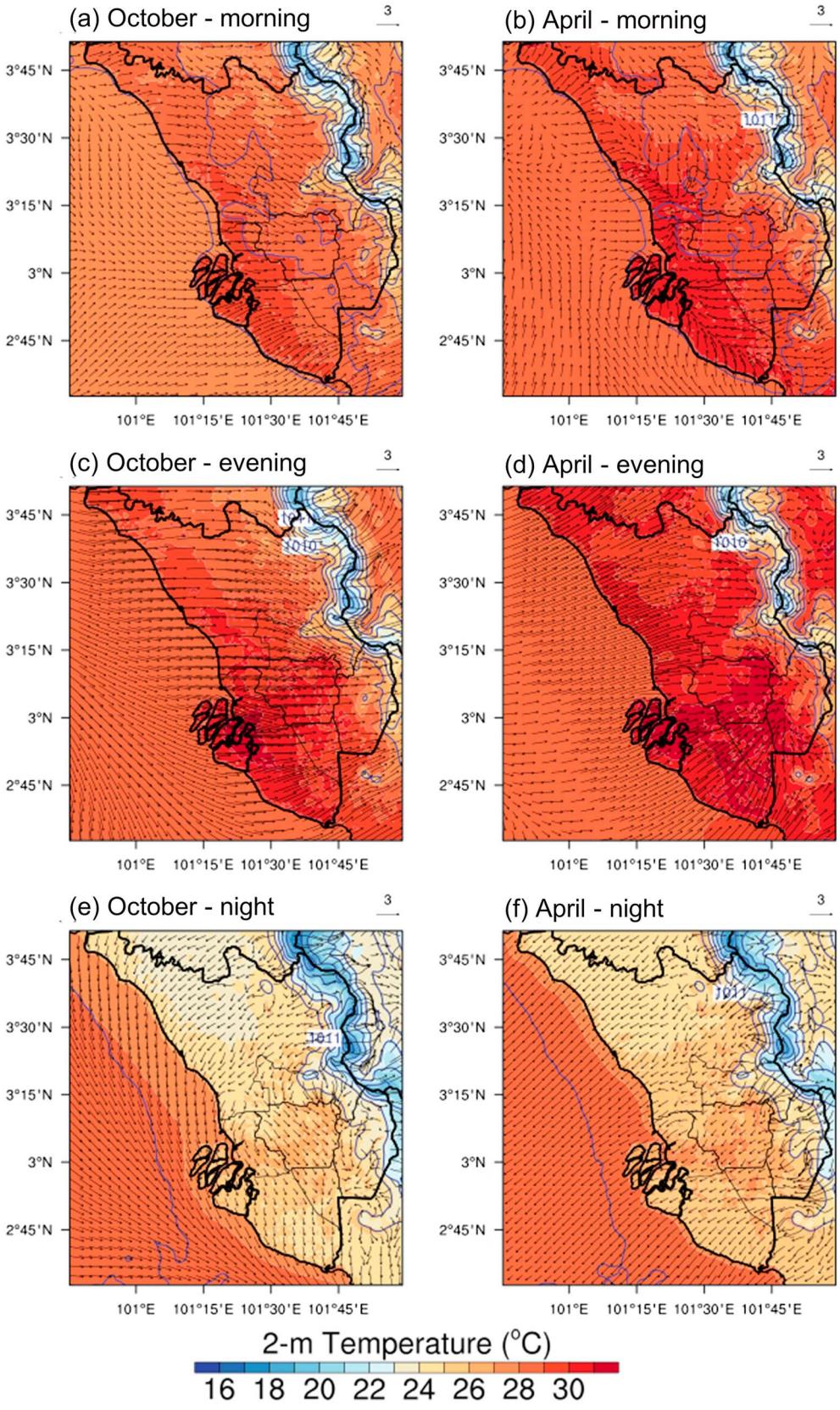

Figure 7. Spatial 10 m wind (m/s), 2 m temperature (°C), and sea level pressure (hPa) profile in the morning, evening, and night for (left column) October and (right column) April.

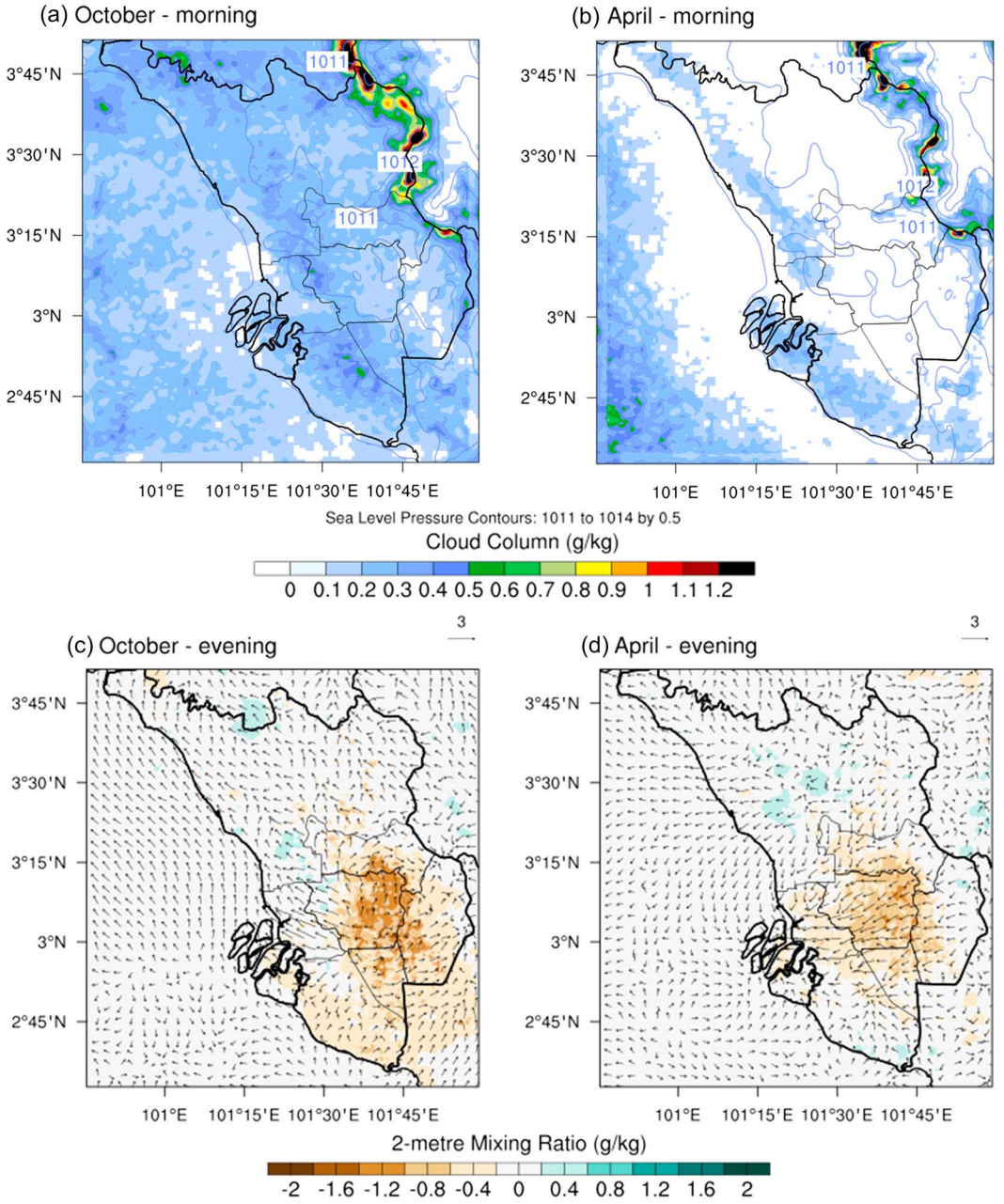

Figure 8. The total cloud column (g/kg) in the morning (0900–1300 MYT) for (a) October and (b) April. Spatial difference of 2 m water vapor mixing ratio (g/kg) and 10 m wind vector (m/s) with noURB case for October (Figure 8c) and April (Figure 8d) at the evening (1500–1800 MYT). Figures 8a and 8b and 8c and 8d have masked out less significant cloud column and response below 0.1 g/kg and mixing ratio response between −0.1 g/kg and 0.1 g/kg, respectively.

Figure 10, explaining the wetness near the coast as seen in Figure 8c. The sea breeze has sustained for an hour longer until 1800 MYT for urbanization case. Subsequently, at 1900 MYT, weaker cold air mass from the mountain top moves downhill over the urban region, parallel with the land breezes that flow toward the Straits of Malacca. The downslope breezes are weakened by urban surface drag and also the weaker night inversion formed as a result of urban heating. This is a common nocturnal phenomenon observed due to urbanization (Giovannini et al., 2013; Kang et al., 2014; Li et al., 2013). The weakening of land breeze as a result of urbanization is prone to the inland progression of air mass from the sea in the following morning.

During the day (from 0800 MYT to 1800 MYT), it is noticed that urbanization enhances the large-scale horizontal advection of air mass on the upper layer from the sea toward the inland mountainous region well

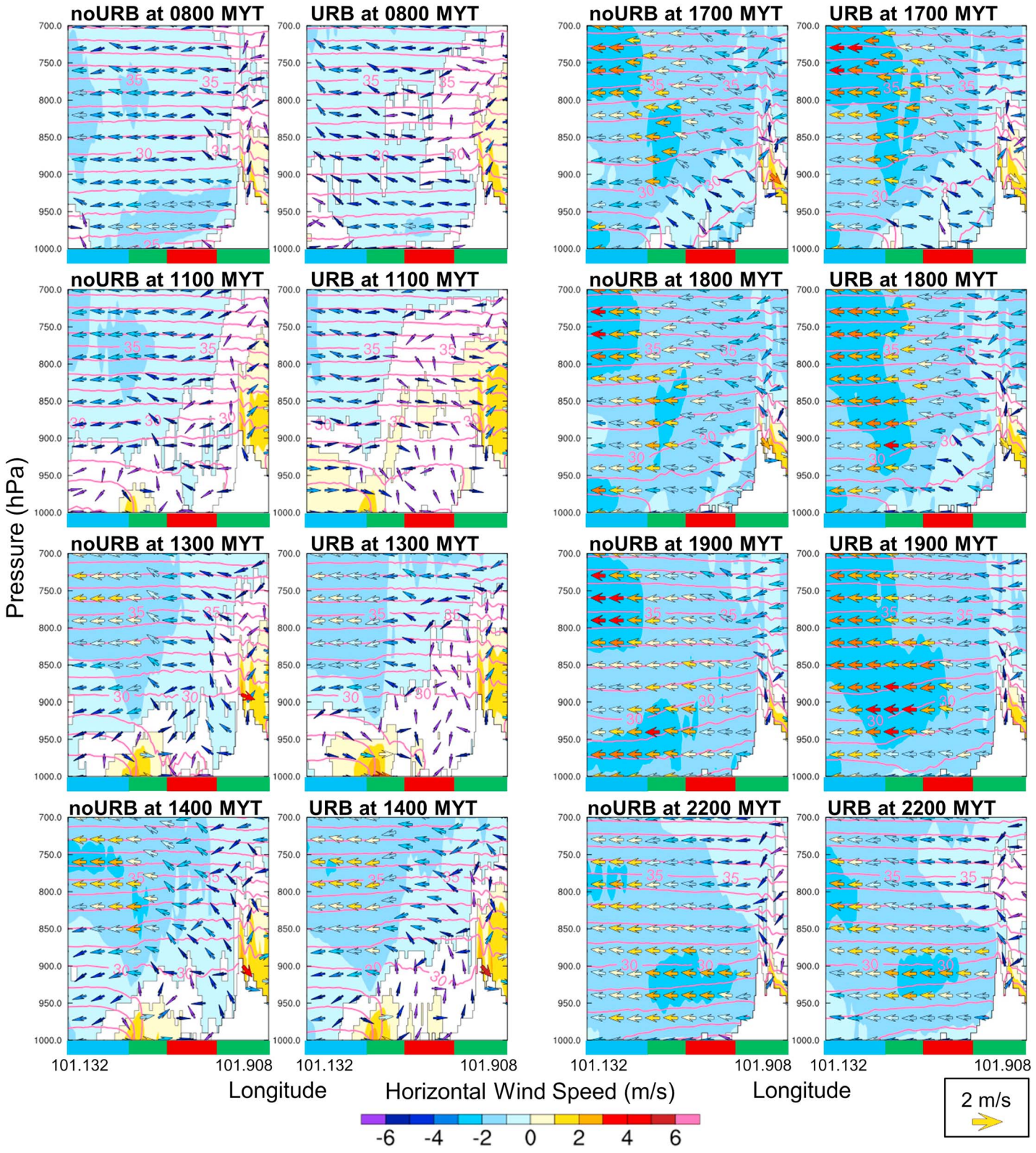

Figure 9. Vertical cross-sectional profile AA′ (cross-sectional profile across the urban, shown in Figure 3) in October for horizontal wind at 1000 MYT, 1100 MYT, 1300 MYT, 1400 MYT, 1700 MYT, 1800 MYT, 1900 MYT, and 2200 MYT. (left) noURB cases and (right) URB cases. Horizontal wind displayed has masked out less significant response between −0.25 m/s and 0.25 m/s. The color bar at the bottom indicates the land use type of the urbanization case along the longitude. The blue for water body, green for nonurban, and red for urban. The vector annotation shown is doubled the actual vector size.

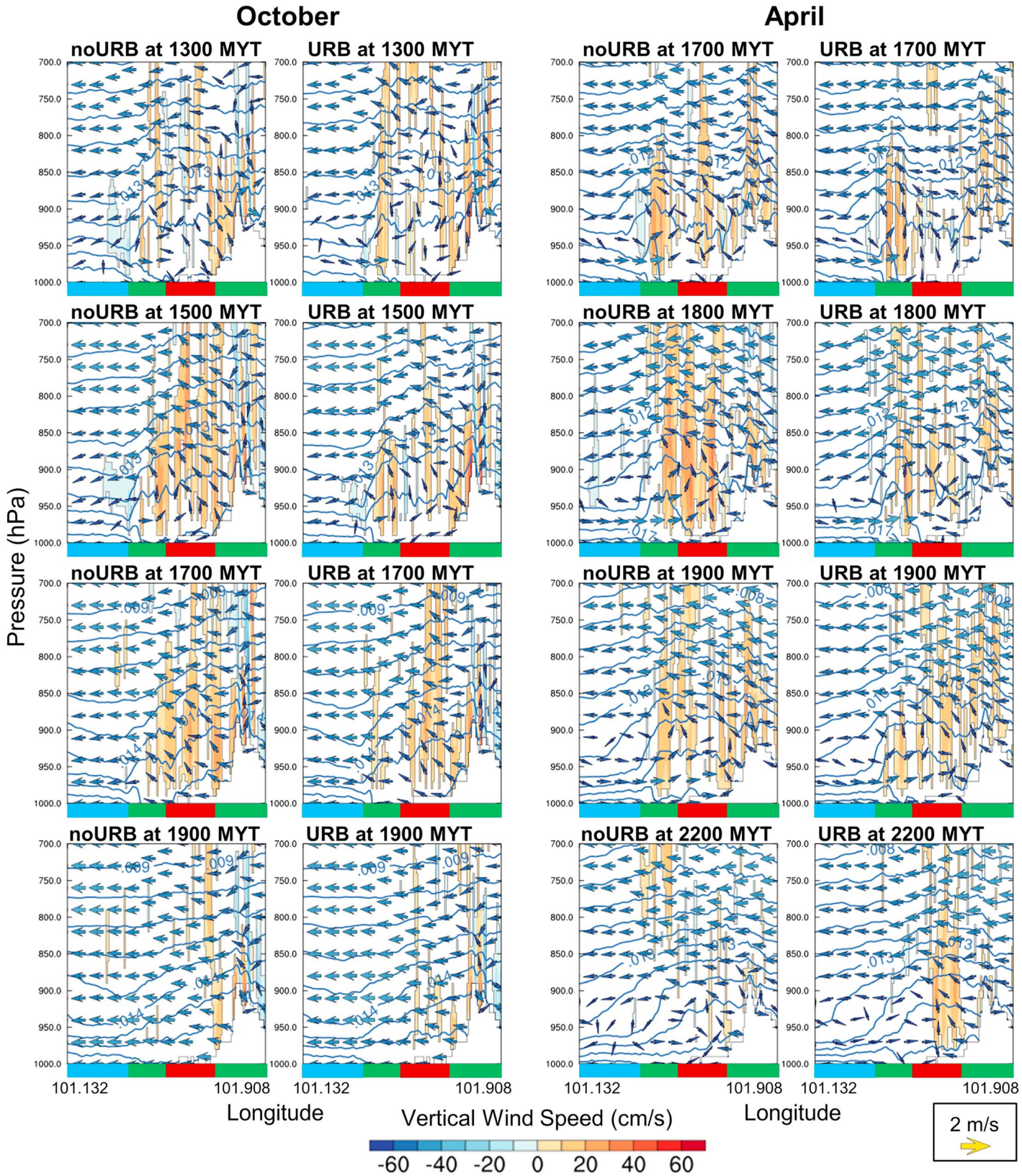

Figure 10. Vertical cross-sectional profile AA′ for vertical wind at 1300 MYT, 1500 MYT, 1700 MYT, and 1900 MYT in October and April. Vertical wind displayed has masked out less significant response between −5.0 cm/s and 5.0 cm/s. The blue contour represents the water vapor mixing ratio in kg/kg. Refer to Figure 9 for detailed information.

before the initiation of sea breeze at 0800 MYT. The weak SBOS is equally observed in the upper boundary layer (1.5 km to 5 km) with less than 2 m s^{-1} from the mountain region as shown in Figure 9. The SBF is lifted as high as 850 hPa, almost one time more than the noURB case. At 1300 MYT as shown in Figure 10, the intensive vertical turbulence generated by the city reduces the tendency of weak opposing SBOS on the hillside of urban. This is more favorable for sea breeze passage inland. The ability of urban-induced circulation to weaken the mountain breeze flowing in the opposite direction of the sea breeze is similarly observed in Beijing agglomeration (Miao et al., 2015). This agrees well with Ji et al. (2013) that found that days with weak SBOS are also conducive to develop deeper SBF. Without the presence of urban region, the meeting of the sea breeze and opposing downhill wind systems leads to the intensification of vertical updraft of the sea breeze to stagnate on the upwind of urban. This is also clearly shown in Figure 10 at 1500 MYT. The prevailing northwesterly synoptic flow across the gap creates the all-day depression on the mountain east in Figure 11. This also explains the tendency of urban-side flow to be drawn toward the east after the opposing SBOS is weakened by the urban thermals. Thus, the connection of both wind systems is the collective contribution the mountain gap and urbanization under weak SBOS condition. At this point, urban land weakens the hillside SBOS and plays a critical role in bridging the two large-scale wind movements from the east and west coast.

4.2.2. April

In April, the land breeze dissipates later around 1000 MYT before sea breeze moves onshore at 1100 MYT, alongside with the up-slope mountain breezes shown in Figure 12. The sea breeze passage enters the urban cluster at 1500 MYT after accumulating sufficient strength (5.71 m s^{-1}). Without the drag imposed by the urban surface (noURB), the sea breezes grow stronger up to 5.87 m/s with a further 2.6 km penetration inland. This resonates well with the urban cool pool formed during the period which weakens the sea breeze strength. The mountain breeze continues to flow toward the urban confluence zone while the core of the sea breeze remains around the upwind coastal region. It is well noted that similar to October, the nocturnal mountain breeze and gap winds reduce in strength due to urbanization. The vertical lifting of the sea breeze is greatly suppressed under 850 hPa as shown in Figures 10 and 12. The unstable Kelvin-Helmholtz billow is also more likely to developed at the top of the sea breeze front under such circumstances (Chemel & Sokhi, 2012; Thompson et al., 2007). At night, a clockwise circulation flow between the surface land breeze and elevated inflow from the sea is induced where subsidence occurs near the Titiwangsa mountain region. This agrees well with the convergence of surface night flow along the Straits of Malacca during the calm intermonsoon period (Fujita et al., 2010). Under the strong SBOS condition, April has shown a clear diurnal circulation of SLB in MC (Hara et al., 2009).

The effect of urbanization on local circulation differs according to the strength of the opposing SBOS in both months. Under the calm and weak synoptic condition, the clear sky and scarce cloud coverage in April enhances the heating of the land surface and the subsequent growth of the sea breeze. The sea breeze flows at a greater magnitude with a prolonged duration (10 h) compared to the October even without urbanization. It is because the lower pressure system is formed near the central of the GKL in April. Despite that, the UHI intensity becomes negative as a result of higher dissipation rate under clear sky in April. The urban cool pool in April has resisted the inflow of sea breeze. Conversely, the positively induced UHI intensity increases the strength of the sea breeze flow in October. Taking account of the synoptic influence, both months have similarly experienced opposing SBOS flow but it is weaker in October than April. Under such circumstances, the strong UHI intensity becomes critical to weaken the opposing SBOS from the hillside in October. Subsequently, sea breeze gains sufficient momentum to push inland and enhances the horizontal advection of sea breeze passage and mountain breeze on a higher elevation height. On the other hand, the strong opposing SBOS in April enhances the gap winds and mountain flows into the GKL region throughout the day as shown in Figure 11. The mountain breeze accelerates after 1500 MYT when the UHI starts to form in place of the cool pool. Therefore, the influence of urbanization on local flow circulation is subjected to both the cloud coverage and the strength and direction of SBOS.

In April, the potential formation of Kelvin-Helmholtz billow is more likely to accumulate at the tail of the SBF and surges the level of secondary pollutants such as ozone in April (Ji et al., 2013). However, during the night, strong gap winds induced by the southwest flow continuously enters the urban region in April. This reveals that the region located near the saddle receives additional gap winds from the east on top of mountain breeze and therefore is better ventilated than October. The exit land breeze flow which responsible of the nocturnal air quality is therefore enhanced in April while impeded in October.

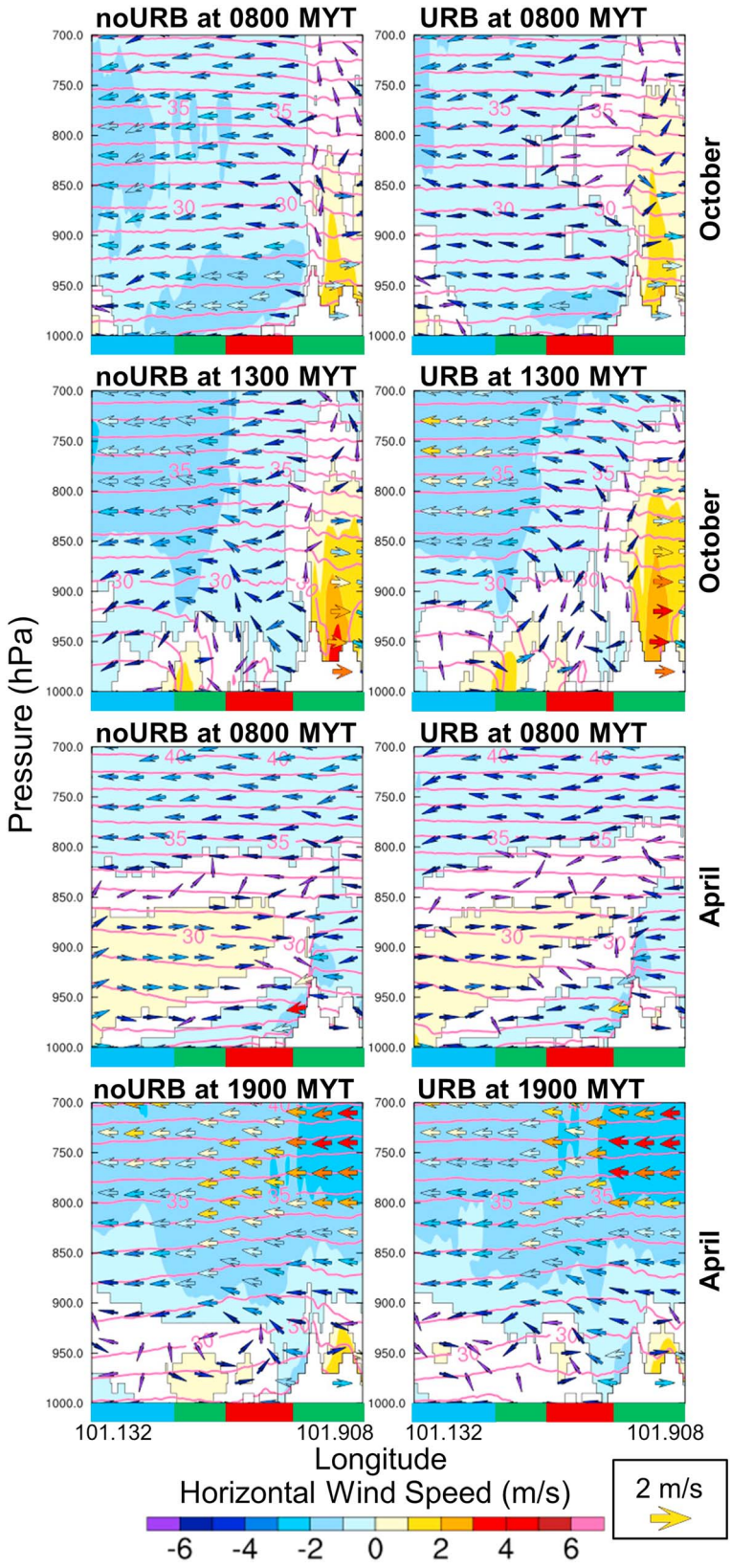

Figure 11. Vertical cross-sectional profile BB′ (cross-sectional profile across the gap, shown in Figure 3) for horizontal wind of noURB at 0800 MYT, 1300 MYT in October and vertical wind case at 0800 MYT, 1900 MYT in April. Refer to Figure 9 for detailed information.

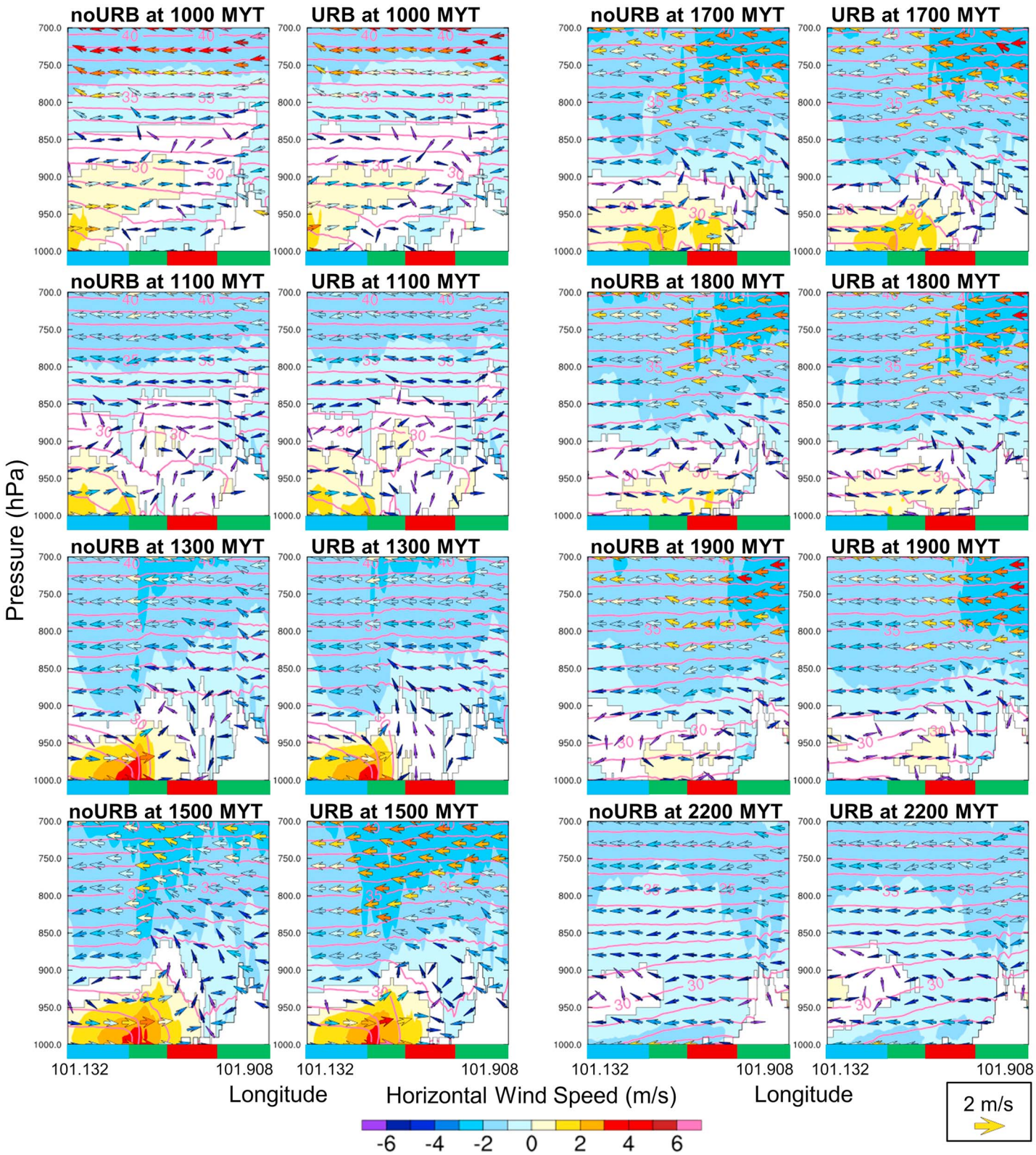

Figure 12. Same as Figure 9 but in April at 1000 MYT, 1100 MYT, 1300 MYT, 1500 MYT, 1700 MYT, 1800 MYT, 1900 MYT, and 2200 MYT.

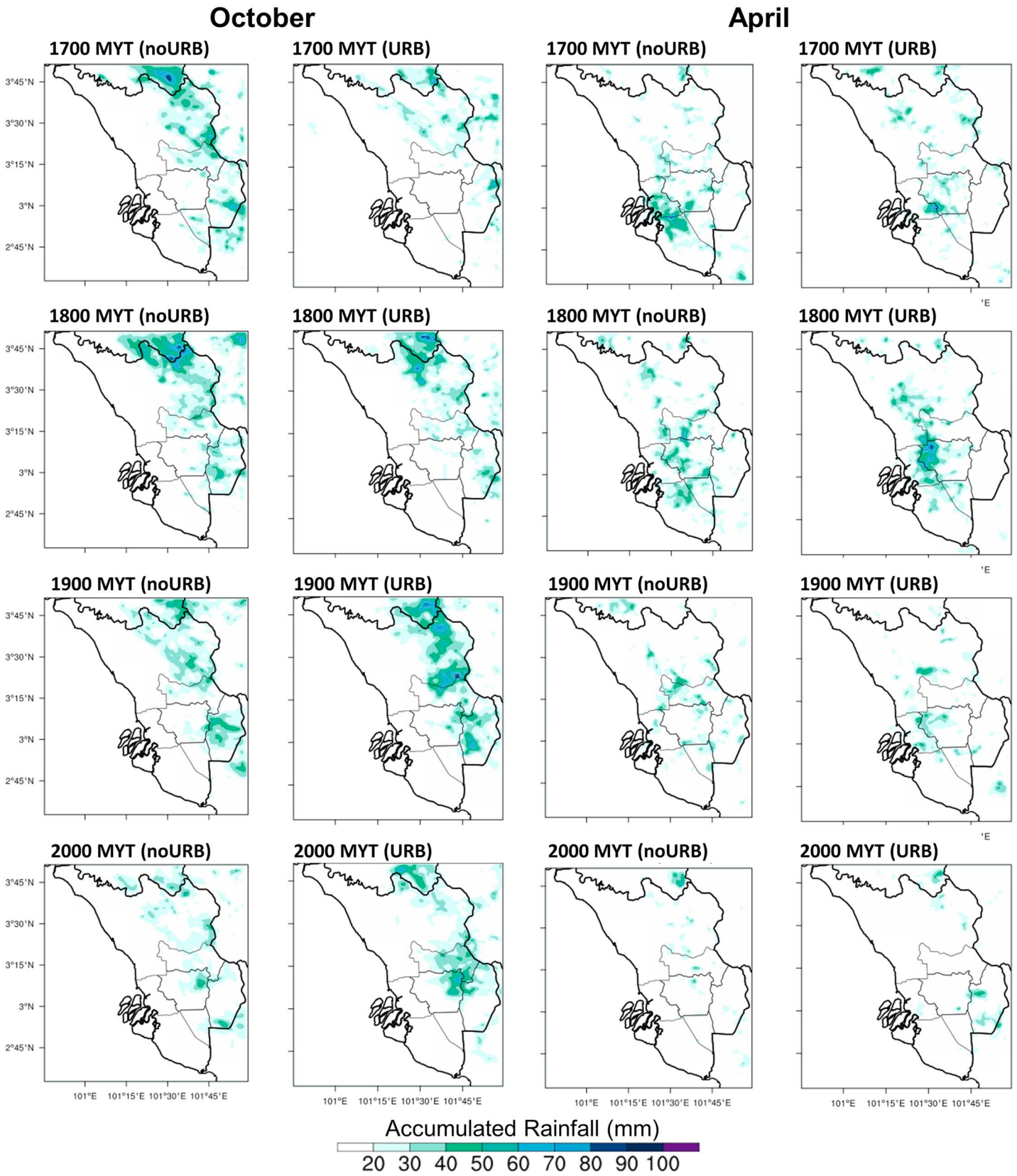

Figure 13. Rain water amount at 1700 MYT, 1800 MYT, 1900 MYT, and 2000 MYT for October and April for noURB and urbanization cases.

4.3. Precipitation Analysis

As discussed earlier, the existence of urban cluster enhances the interaction of sea breeze on the upper boundary layer connecting the sea and the mountain top in October. The moisture influx into the higher boundary layer on the windward side of the mountain suggests potential modification on the precipitation profile. The resulting inflow of moist air from the sea with the forced convection at the steep mountain slope is favorable for the formation of tropical convective raining (Mori et al., 2004; Sato & Kimura, 2005) and also the neighboring West Sumatra (Sasaki et al., 2004). Figure 13 hence shows a tendency to precipitate on the hilly side of the urban during the peak hours from 1700 MYT to 2000 MYT. Urbanization produces comparable total accumulated rainfall with noURB but the precipitation arrives 2 h later as shown in Figure 13. This is in-sync with the delayed retreat of sea breeze and the subsequent initiation of the mountain breeze. The effect of urbanization on precipitation is found to be largely dependent on the urban influence on the evolution of moisture-rich sea breeze. Such delay is equally observed due to the prolonged effect of sea breeze in Greater Beijing Metropolitan Area (Zhong & Yang, 2015).

In April, the hourly total rainfall amount in Figure 13 notes that the rainfall is more concentrated on the upwind of urban. This is highly associated with the confrontation of the weaker sea breeze system and the mountain flow from the east during the strong sea breeze front month as shown in Figure 12. The gap between mountain range has enhanced the interaction of propagating wind systems from each side of the peninsula which initiates the thunderstorm in GKL during the calm synoptic condition (Joseph et al., 2008; Sow et al., 2011; Teo et al., 2011). The precipitation concentrates on the upwind region of urban due to the buoyancy lifting induced by the UHI at 1800 MYT as shown in Figure 10. The downdraft intensity might be also contributed by several other factors including the anthropogenic heat, type of urban surfaces, and the amount of cloud condensation nuclei especially in the polluted urban (Han, Baik, & Lee, 2014; Kaufmann et al., 2007; Sharma et al., 2016). This finding has shown that urbanization displaces and intensifies the precipitation activities as observed in many previous studies (Dixon & Mote, 2003; Pathirana et al., 2014; Thielen et al., 2000).

The result emphasizes the evolution of sea breeze movement on the precipitation profile (Sakurai et al., 2005). The presence of urban greatly modifies the sea breeze passage which is later reflected in the late afternoon precipitation pattern. However, it should be aware that the ability of simulation model to predict the short time-span convective precipitation is still limited and under continual assessment and improvement (Bhatt et al., 2016).

5. Conclusions

The effect of urbanization on local topographic circulation is studied with WRF simulation model at the most developed cluster in GKL, Malaysia. The role of the synoptic condition on the interaction of urban heating and topographic-induced circulation is also evaluated between two intermonsoonal months (April and October). The ensemble model performance of WRF is first evaluated against sounding data and near-surface weather parameters within the period of study. The selection of MYJ PBL local scheme is able to realistically produces the vertical temperature and wind profile especially in the atmospherically stable April month. The allocation of thermal roughness length to respective land use also improves the ability of the Eta similarity theory surface layer scheme (coupled with MYJ PBL scheme) to estimate the heat transfer coefficient and hence better determines the near-surface condition. Three combinations of micro-physics and cumulus schemes are run to reduce the erratic signal of near-surface weather condition and precipitation field.

The diurnal heating of urban surface is stronger at night than the day, recording around 1.4°C in both months. Unlike the nocturnal UHI intensity that is rather consistent between the months, the daytime UHI intensity varies between October and April. Hot bias is observed in October while April month produces a colder surface in midday (0900 MYT–1300 MYT) compared to the noURB case. The negative UHI intensity in April during this period is mainly attributed to the higher heating rate of the vegetation cover influenced by the previous day precipitation. The differential heating rate is further enhanced in the clear-sky condition of April. Later in 1500 MYT to 1800 MYT, larger positive UHI intensity developed in October is to carry more moisture to the upwind region of urban. This occurs concurrent to the initiation hours of late afternoon convective raining and therefore confirmed the association of urbanization with precipitation.

The local influence of urbanization generally depends on the strength of the urban heating and also SBOS. GKL experiences opposing synoptic flow which subsequently forms the SBF in both months. During the day, urban thermals tend to reduce the strength of the weak opposing SBOS in October. This enhances the magnitude of the sea breeze flow. The large inflow of moisture-bearing sea breeze toward the higher ground therefore generates larger amount of precipitation on the downwind of the urban region. On the other hand, the urban cool pool formed under the clear sky decelerates the sea breeze in April. The strong opposing SBOS in April further suppresses inland propagation of the sea breeze. Its accelerated core stalls over the upwind region before the urban where the convective precipitation occurs. The effect of urbanization on precipitation is hence found to be largely dependent on its influence on the evolution of moisture-rich sea breeze.

The nocturnal effect of urbanization is less variant between the months. The nocturnal land and mountain breezes decelerate due to the urban drag and the intense urban heating effect at night. Nevertheless, strong opposing SBOS in April significantly enhances the land breeze and gap winds in April and suggested better ventilation in GKL during the night compared to the October month. The analyses therefore conclude that the influence of urbanization on local regional weather is highly dependent on the synoptic condition during the day while the local thermal response is most apparent during the night.

The availability data limit the verification temporal and spatial of vertical profile but each verification step complements each other well to confirm the robustness of the model. However, the discrepancies of vertical wind speed and surface humidity profile suggest that the convective mechanism of the model could be better improved. It is noteworthy that this study conducted is a first step to identify the influence of urbanization on the urban boundary climate in terms of thermal, wind circulation, and precipitation condition in the particular year of weak precipitation anomaly. It should not be generalized to represent the typical response of the urbanization. With the existing findings, the chemical driver for the investigation of the effect of urbanization on the formation and transportation of the local urban pollutant can be incorporated and this will be pursued in the future.

Acknowledgments

The authors would like thank the Ministry of Science Technology and Innovation (MOSTI) of Malaysia for providing financial support for this research work. This work is partly sponsored under contract 06-02-12-SF0346. The authors would also like to thank University of Nottingham Malaysia Campus for awarding a research scholarship. We are also grateful for access to the University of Nottingham High Performance Computing Facility. The data for TRMM 3B42 (TMPA) data are available from https://pmm.nasa.gov/data-access/downloads/trmm. The ERA-interim data were obtained from http://apps.ecmwf.int/datasets/data/interim-full-daily/. The ground measurement and sounding data were obtained from the Department of Environment (DOE) Malaysia (https://www.doe.gov.my/portalv1/en/) and Malaysia Meteorological Department (MMD) (http://www.met.gov.my/en/web/metmalaysia/publicservices/eservices/datainformationapplication) available upon request.

References

Arnfield, A. J. (2003). Two decades of urban climate research: A review of turbulence, exchanges of energy and water, and the urban heat island. *International Journal of Climatology*, *23*(1), 1–26. https://doi.org/10.1002/joc.859

Balzarini, A., Angelini, F., Ferrero, L., Moscatelli, M., Perrone, M. G., Pirovano, G., … Bolzacchini, E. (2014). Sensitivity analysis of PBL schemes by comparing WRF model and experimental data. *Geoscientific Model Development Discussion*, *7*(5), 6133–6171. https://doi.org/10.5194/gmdd-7-6133-2014

Barlow, J. F. (2014). Progress in observing and modelling the urban boundary layer. *Urban Climate*, *10*, 216–240. https://doi.org/10.1016/j.uclim.2014.03.011

Berner, J., Ha, S.-Y., Hacker, J. P., Fournier, A., & Snyder, C. (2011). Model uncertainty in a mesoscale ensemble prediction system: Stochastic versus multiphysics representations. *Monthly Weather Review*, *139*(6), 1972–1995. https://doi.org/10.1175/2010MWR3595.1

Bhatt, B. C., Sobolowski, S., & Higuchi, A. (2016). Simulation of diurnal rainfall variability over the Maritime Continent with a high-resolution regional climate model. *Journal of the Meteorological Society of Japan*, *94A*(0), 89–103. https://doi.org/10.2151/jmsj.2015-052

Chang, C. P., Wang, Z., McBride, J., & Liu, C. H. (2005). Annual cycle of Southeast Asia—Maritime continent rainfall and the asymmetric monsoon transition. *Journal of Climate*, *18*(2), 287–301. https://doi.org/10.1175/JCLI-3257.1

Chemel, C., & Sokhi, R. S. (2012). Response of London's urban heat island to a marine air intrusion in an easterly wind regime. *Boundary-Layer Meteorology*, *144*(1), 65–81. https://doi.org/10.1007/s10546-012-9705-x

Chen, F., Kusaka, H., Bornstein, R., Ching, J., Grimmond, C. S. B., Grossman-Clarke, S., … Zhang, C. (2011). The integrated WRF/urban modelling system: Development, evaluation, and applications to urban environmental problems. *International Journal of Climatology*, *31*(2), 273–288. https://doi.org/10.1002/joc.2158

Chen, F., Miao, S., Tewari, M., Bao, J. W., & Kusaka, H. (2011). A numerical study of interactions between surface forcing and sea breeze circulations and their effects on stagnation in the greater Houston area. *Journal of Geophysical Research*, *116*, D12105. https://doi.org/10.1029/2010JD015533

Chen, F., & Zhang, Y. (2009). On the coupling strength between the land surface and the atmosphere: From viewpoint of surface exchange coefficients. *Geophysical Research Letters*, *36*, L10404. https://doi.org/10.1029/2009GL037980

Cheng, W. Y. Y., & Steenburgh, W. J. (2005). Evaluation of surface sensible weather forecasts by the WRF and the Eta models over the western United States. *Weather and Forecasting*, *20*(5), 812–821. https://doi.org/10.1175/WAF885.1

Chow, W. T. L., & Roth, M. (2003). Temporal dynamics of the urban heat island of Singapore. *International Journal of Climatology*, *26*(15), 2243–2260. https://doi.org/10.1002/joc.1364

Collier, C. G. (2006). The impact of urban areas on weather. *Quarterly Journal of the Royal Meteorological Society*, *132*(614), 1–25. https://doi.org/10.1256/qj.05.199

Cruz, F. T., & Narisma, G. T. (2016). WRF simulation of the heavy rainfall over Metropolitan Manila, Philippines during tropical cyclone Ketsana: A sensitivity study. *Meteorology and Atmospheric Physics*, *128*(4), 415–428. https://doi.org/10.1007/s00703-015-0425-x

Dandou, A., Tombrou, M., & Nikolaos, S. (2009). The influence of the City of Athens on the evolution of the sea-breeze front. *Boundary-Layer Meteorology*, *131*(1), 35–51. https://doi.org/10.1007/s10546-008-9306-x

Daniels, E., Lenderink, G., Hutjes, R., & Holtslag, A. (2016). Relative impacts of land use and climate change on summer precipitation in the Netherlands. *Hydrology and Earth System Sciences*, *20*(10), 4129–4142. https://doi.org/10.5194/hess-20-4129-2016

Dee, D. P., Uppala, S. M., Simmons, A. J., Berrisford, P., Poli, P., Kobayashi, S., … Vitart, F. (2011). The ERA-Interim reanalysis: Configuration and performance of the data assimilation system. *Quarterly Journal of the Royal Meteorological Society*, *137*(656), 553–597. https://doi.org/10.1002/qj.828

Department of Environment Malaysia (2016). Chronology of haze episodes in Malaysia, 1–3. Retrieved from https://www.doe.gov.my/portalv1/en/info-umum/info-kualiti-udara/kronologi-episod-jerebu-di-malaysia/319123 (Accessed 21 October 2016).

Ding, Y., & Chan, J. C. L. (2005). The East Asian summer monsoon: An overview. *Meteorology and Atmospheric Physics*, *89*(1-4), 117–142. https://doi.org/10.1007/s00703-005-0125-z

Diong, J. Y., Yip, W. S., MatAdam, M. K., Chang, N. K., Yunus, F., & Abdullah, M. H. (2015). The definitions of the southwest monsoon climatological onset and withdrawal over Malaysian region. *Malaysian Meteorology Department*, *3*, 1–30.

Dixon, P. G., & Mote, T. L. (2003). Patterns and causes of Atlanta's urban heat island–initiated precipitation. *Journal of Applied Meteorology*, *42*(9), 1273–1284. https://doi.org/10.1175/1520-0450(2003)042%3C1273:PACOAU%3E2.0.CO;2

Freitas, E. D., Rozoff, C. M., Cotton, W. R., & Dias, P. L. S. (2006). Interactions of an urban heat island and sea-breeze circulations during winter over the metropolitan area of São Paulo, Brazil. *Boundary-Layer Meteorology*, *122*(1), 43–65. https://doi.org/10.1007/s10546-006-9091-3

Fujita, M., Kimura, F., & Yoshizaki, M. (2010). Morning precipitation peak over the Strait of Malacca under a calm condition. *Monthly Weather Review*, *138*(4), 1474–1486. https://doi.org/10.1175/2009MWR3068.1

Gedzelman, S. D., Austin, S., Cermak, R., Stefano, N., Partridge, S., Quesenberry, S., & Robinson, D. A. (2003). Mesoscale aspects of the urban heat island around New York City. *Theoretical and Applied Climatology*, *75*(1-2), 29–42. https://doi.org/10.1007/s00704-002-0724-2

Giovannini, L., Zardi, D., de Franceschi, M., & Chen, F. (2013). Numerical simulations of boundary-layer processes and urban-induced alterations in an Alpine valley. *International Journal of Climatology*, *34*(4), 1111–1131. https://doi.org/10.1002/joc.3750

Grossman-Clarke, S., Liu, Y., Zehnder, J. A., & Fast, J. D. (2008). Simulations of the urban planetary boundary layer in an arid metropolitan area. *Journal of Applied Meteorology and Climatology*, *47*(3), 752–768. https://doi.org/10.1175/2007JAMC1647.1

Han, J.-Y., Baik, J.-J., & Lee, H. (2014). Urban impacts on precipitation. *Asia-Pacific Journal of Atmospheric Sciences*, *50*(1), 17–30. https://doi.org/10.1007/s13143-014-0016-7

Hara, M., Yoshikane, T., Takahashi, H. G., Kimura, F., Noda, A., & Tokioka, T. (2009). Assessment of the diurnal cycle of precipitation over the Maritime Continent simulated by a 20 km mesh GCM using TRMM PR data. *Journal of the Meteorological Society of Japan*, *87A*, 413–424. https://doi.org/10.2151/jmsj.87A.413

Hidalgo, J., Pigeon, G., & Masson, V. (2008). Urban-breeze circulation during the CAPITOUL experiment: Numerical simulations. *Meteorology and Atmospheric Physics*, *102*(3-4), 243–262. https://doi.org/10.1007/s00703-008-0345-0

Hong, S.-Y., Dudhia, J., & Chen, S.-H. (2004). A revised approach to ice microphysical processes for the bulk parameterization of clouds and precipitation. *Monthly Weather Review*, *132*(1), 103–120. https://doi.org/10.1175/1520-0493(2004)132%3C0103:ARATIM%3E2.0.CO;2

Hong, S.-Y., & Lim, J.-O. J. (2006). The WRF single-moment 6-class microphysics scheme (WSM6). *Journal Korean Meteorological Society*, *42*(2), 129–151.

Inness, A., Benedetti, A., Flemming, J., Huijnen, V., Kaiser, J. W., Parrington, M., & Remy, S. (2015). The ENSO signal in atmospheric composition fields: Emission-driven versus dynamically induced changes. *Atmospheric Chemistry and Physics*, *15*(15), 9083–9097. https://doi.org/10.5194/acp-15-9083-2015

Janjic, Z. I. (1994). The step-mountain Eta coordinate model: Further developments of convection viscous sublayer, turbulence closure schemes. *Monthly Weather Review*, *122*(5), 927–945. https://doi.org/10.1175/1520-0493(1994)122%3C0927:TSMECM%3E2.0.CO;2

Jauregui, E. (1997). Heat island development in Mexico City. *Atmospheric Environment*, *31*(22), 3821–3831. https://doi.org/10.1016/S1352-2310(97)00136-2

Jauregui, E., Godinez, L., & Cruz, F. (1992). Aspects of heat-island development in Guadalajara, Mexico. *Atmospheric Environment*, *26B*(3), 391–396.

Ji, H. E., Lee, S. H., & Lee, H. W. (2013). Characteristics of sea breeze front development with various synoptic conditions and its impact on lower troposphere ozone formation. *Advances in Atmospheric Sciences*, *30*(5), 1461–1478. https://doi.org/10.1007/s00376-013-2256-3

Jiménez, P. A., & Dudhia, J. (2012). Improving the representation of resolved and unresolved topographic effects on surface wind in the wrf model. *Journal of Applied Meteorology and Climatology*, *51*(2), 300–316. https://doi.org/10.1175/JAMC-D-11-084.1

Jiménez, P. A., Dudhia, J., González-Rouco, J. F., Montávez, J. P., García-Bustamante, E., Navarro, J., … Muñoz-Roldán, A. (2013). An evaluation of WRF's ability to reproduce the surface wind over complex terrain based on typical circulation patterns. *Journal of Geophysical Research: Atmospheres*, *118*, 7651–7669. https://doi.org/10.1002/jgrd.50585

Joseph, B., Bhatt, B. C., Koh, T. Y., & Chen, S. (2008). Sea breeze simulation over the Malay Peninsula in an intermonsoon period. *Journal of Geophysical Research*, *113*, D20122. https://doi.org/10.1029/2008JD010319

Kang, H. Q., Zhu, B., Zhu, T., Sun, J. L., & Ou, J. J. (2014). Impact of Megacity Shanghai on the urban heat-island effects over the Downstream City Kunshan. *Boundary-Layer Meteorology*, *152*(3), 411–426. https://doi.org/10.1007/s10546-014-9927-1

Kaufmann, R. K., Seto, K. C., Schneider, A., Liu, Z., Zhou, L., & Wang, W. (2007). Climate response to rapid urban growth: Evidence of a human-induced precipitation deficit. *Journal of Climate*, *20*(10), 2299–2306. https://doi.org/10.1175/JCLI4109.1

Kikuchi, K., & Wang, B. (2008). Diurnal precipitation regimes in the global tropics. *Journal of Climate*, *21*(11), 2680–2696. https://doi.org/10.1175/2007JCLI2051.1

Kim, Y.-H., & Baik, J.-J. (2002). Maximum urban Heat Island intensity in Seoul. *Journal of Applied Meteorology*, *41*(6), 651–659. https://doi.org/10.1175/1520-0450(2002)041%3C0651:MUHIII%3E2.0.CO;2

Kusaka, H., Nawata, K., Suzuki-Parker, A., Takane, Y., & Furuhashi, N. (2014). Mechanism of precipitation increase with urbanization in Tokyo as revealed by ensemble climate simulations. *Journal of Applied Meteorology and Climatology*, *53*(4), 824–839. https://doi.org/10.1175/JAMC-D-13-065.1

Lai, L.-W., & Cheng, W.-L. (2009). Air quality influenced by urban heat island coupled with synoptic weather patterns. *Science of the Total Environment*, *407*(8), 2724–2733. https://doi.org/10.1016/j.scitotenv.2008.12.002

Lemonsu, A., & Masson, V. (2002). Simulation of a summer urban breeze over Paris. *Boundary-Layer Meteorology*, *104*(3), 463–490. https://doi.org/10.1023/A:1016509614936

Li, X. X., Koh, T. Y., Entekhabi, D., Roth, M., Panda, J., & Norford, L. K. (2013). A multi-resolution ensemble study of a tropical urban environment and its interactions with the background regional atmosphere. *Journal of Geophysical Research: Atmospheres*, *118*, 9804–9818. https://doi.org/10.1002/jgrd.50795

Li, X.-X., Koh, T.-Y., Panda, J., & Norford, L. K. (2016). Impact of urbanization patterns on the local climate of a tropical city Singapore: An ensemble study. *Journal of Geophysical Research: Atmospheres*, *121*, 4386–4403. https://doi.org/10.1002/2015JD024452

Lin, C.-Y., Chen, F., Huang, J. C., Chen, W.-C., Liou, Y.-A., Chen, W.-N., & Liu, S.-C. (2008). Urban heat island effect and its impact on boundary layer development and land–sea circulation over northern Taiwan. *Atmospheric Environment*, *42*(22), 5635–5649. https://doi.org/10.1016/j.atmosenv.2008.03.015

Lin, N.-H., Tsay, S.-C., Maring, H. B., Yen, M.-C., Sheu, G.-R., Wang, S.-H., … Liu, G.-R. (2013). An overview of regional experiments on biomass burning aerosols and related pollutants in Southeast Asia: From BASE-ASIA and the Dongsha experiment to 7-SEAS. *Atmospheric Environment*, *78*, 1–19. https://doi.org/10.1016/j.atmosenv.2013.04.066

Lin, Y.-L., Farley, R. D., & Orville, H. D. (1983). Bulk parameterization of snow dield in a cloud model. *American Meteorological Society*, *22*, 1065–1092.

Lo, J. C. F., Lau, A. K. H., Fung, J. C. H., & Chen, F. (2006). Investigation of enhanced cross-city transport and trapping of air pollutants by coastal and urban land-sea breeze circulations. *Journal of Geophysical Research*, *111*, D14104. https://doi.org/10.1029/2005JD006837

Loughner, C. P., Allen, D. J., Zhang, D.-L., Pickering, K. E., Dickerson, R. R., & Landry, L. (2012). Roles of urban tree canopy and buildings in urban heat island effects: Parameterization and preliminary results. *Journal of Applied Meteorology and Climatology*, *51*(10), 1775–1793. https://doi.org/10.1175/JAMC-D-11-0228.1

Mass, C., & Ovens, D. (2011). Fixing WRF's high speed wind bias: A new subgrid scale drag parameterization and the role of detailed verification, in *24th Conf. on Weather and Forecasting/20th Conf. on Numerical Weather Prediction* (p. 9B.6). Seattle, WA: American Meteorological Society.

McPhaden, M. J. (2004). Evolution of the 2002/03 El Niño. *Bulletin of the American Meteorological Society*, *85*(5), 677–695. https://doi.org/10.1175/BAMS-85-5-677

Mellor, G. L., & Yamada, T. (1982). Development of a turbulence closure model for geophysical fluid problems. *Reviews of Geophysics Space Physics*, *20*(4), 851–875. https://doi.org/10.1029/RG020i004p00851

Miao, S., Chen, F., LeMone, M. A., Tewari, M., Li, Q., & Wang, Y. (2009). An observational and modeling study of characteristics of urban heat island and boundary layer structures in Beijing. *Journal of Applied Meteorology and Climatology*, *48*(3), 484–501. https://doi.org/10.1175/2008JAMC1909.1

Miao, Y., Liu, S., Zheng, Y., Wang, S., & Chen, B. (2015). Numerical study of the effects of topography and urbanization on the local atmospheric circulations over the Beijing-Tianjin-Hebei, China. *Advances in Meteorology*, *2015*, 1–16. https://doi.org/10.1155/2015/397070

Mlawer, E. J., Taubman, S. J., Brown, P. D., Iacono, M. J., & Clough, S. A. (1997). Radiative transfer for inhomogeneous atmospheres: RRTM, a validated correlated-k model for the longwave. *Journal of Geophysical Research*, *102*(D14), 16663–16682. https://doi.org/10.1029/97JD00237

Mori, S., Jun-Ichi, H., Tauhid, Y. I., Yamanaka, M. D., Okamoto, N., Murata, F., … Sribimawati, T. (2004). Diurnal land–sea rainfall peak migration over Sumatera Island, Indonesian Maritime Continent, observed by TRMM Satellite and Intensive Rawinsonde Soundings. *Monthly Weather Review*, *132*(8), 2021–2039. https://doi.org/10.1175/1520-0493(2004)132%3C2021:DLRPMO%3E2.0.CO;2

Morris, C. J. G., Simmonds, I., & Plummer, N. (2001). Quantification of the influences of wind and cloud on the nocturnal urban heat island of a large city. *Journal of Applied Meteorology*, *40*(2), 169–182. https://doi.org/10.1175/1520-0450(2001)040%3C0169:QOTIOW%3E2.0.CO;2

Morris, K. I., Chan, A., Morris, K. J. K., Ooi, M. C. G., Oozeer, M. Y., Abakr, Y. A., … Mohammed, I. Y. (2017). Urbanisation and urban climate of a tropical conurbation, Klang Valley, Malaysia. *Urban Climate*, *19*(December), 54–71. https://doi.org/10.1016/j.uclim.2016.12.002

Moten, S., Yunus, F., Ariffin, M., Burham, N., Jeong Yik, D., Mat Adam, M. K., & Weng Sang, Y. (2014). Statistics of northeast monsoon onset, withdrawal and cold surges in Malaysia, Petaling Jaya.

NOAA (2017). Multivariate ENSO Index (MEI), ESRL Syst. Res. Lab. Phys. Sci. Div. Retrieved from https://www.esrl.noaa.gov/psd/enso/mei/. (Accessed 25 May 2017).

Ohashi, Y., & Kida, H. (2002). Effects of mountains and urban areas on daytime local-circulations in the Osaka and Kyoto regions. *Journal of the Meteorological Society of Japan*, *80*(4), 539–560. https://doi.org/10.2151/Jmsj.80.539

Oke, T. R. (1976). The distinction between canopy and boundary—Layer urban heat islands. *Atmosphere (Basel).*, *14*(4), 37–41. https://doi.org/10.1080/00046973.1976.9648422

Oke, T. R. (1987). *Boundary Layer Climates*, (2nd ed.). London: Routledge.

Oke, T. R. (1995). The heat island of the urban boundary layer: Characteristics, causes and effects. In J. E. Cermak, et al. (Eds.), *Wind climate in cities* (pp. 81–107). Netherlands: Kluwer Academic. https://doi.org/10.1007/978-94-017-3686-2_5

Oke, T. R., & Maxwell, G. B. (1975). Urban heat island dynamics in Montreal and Vancouver. *Atmospheric Environment*, *9*(2), 191–200. https://doi.org/10.1016/0004-6981(75)90067-0

Oki, T., & Musiake, K. (1994). Seasonal change of the diurnal cycle of precipitation over Japan and Malaysia.Pdf. *Journal of Applied Meteorology*, *33*(12), 1445–1463. https://doi.org/10.1175/1520-0450(1994)033%3C1445:SCOTDC%3E2.0.CO;2

Ooi, M. C. G., Chan, A., Ashfold, M. J., Morris, K. I., Oozeer, M. Y., & Salleh, S. A. (2017). Numerical study on effect of urban heating on local climate during calm inter-monsoon period in greater Kuala Lumpur, Malaysia. *Urban Climate*, *20*, 228–250. https://doi.org/10.1016/j.uclim.2017.04.010

Pathirana, A., Denekew, H. B., Veerbeek, W., Zevenbergen, C., & Banda, A. T. (2014). Impact of urban growth-driven landuse change on microclimate and extreme precipitation - a sensitivity study. *Atmospheric Research*, *138*(2014), 59–72. https://doi.org/10.1016/j.atmosres.2013.10.005

Pichelli, E., Ferretti, R., Cacciani, M., Siani, A. M., Ciardini, V., & Di Iorio, T. (2014). The role of urban boundary layer investigated with high-resolution models and ground-based observations in Rome area: A step towards understanding parameterization potentialities. *Atmospheric Measurement Techniques*, *7*(1), 315–332. https://doi.org/10.5194/amt-7-315-2014

Qian, T., Epifanio, C. C., & Zhang, F. (2012). Topographic effects on the tropical land and sea breeze. *Journal of the Atmospheric Sciences*, *69*(1), 130–149. https://doi.org/10.1175/JAS-D-11-011.1

Reid, J. S., Hyer, E. J., Johnson, R. S., Holben, B. N., Yokelson, R. J., Zhang, J., … Liew, S. C. (2013). Observing and understanding the Southeast Asian aerosol system by remote sensing: An initial review and analysis for the Seven Southeast Asian Studies (7SEAS) program. *Atmospheric Research*, *122*, 403–468. https://doi.org/10.1016/j.atmosres.2012.06.005

Roth, M. (2007). Review of urban climate research in (sub)tropical regions. *International Journal of Climatology*, *27*(14), 1859–1873. https://doi.org/10.1002/joc

Ryu, Y. H., & Baik, J. J. (2013). Daytime local circulations and their interactions in the Seoul metropolitan area. *Journal of Applied Meteorology and Climatology*, *52*(4), 784–801. https://doi.org/10.1175/JAMC-D-12-0157.1

Sakurai, N., Murata, F., Yamanaka, M. D., Mori, S., Hamada, J.-I., Hashiguchi, H., … Suhardi, B. (2005). Diurnal cycle of cloud system migration over Sumatera Island. *Journal of the Meteorological Society of Japan*, *83*(5), 835–850. https://doi.org/10.2151/jmsj.83.835

Salimun, E., Tangang, F., & Juneng, L. (2010). Simulation of heavy precipitation episode over eastern Peninsular Malaysia using MM5: Sensitivity to cumulus parameterization schemes. *Meteorology and Atmospheric Physics*, *107*(1-2), 33–49. https://doi.org/10.1007/s00703-010-0067-y

Sani, S. (1977). Aspects of air pollution climatology in the Kuala Lumpur-Petaling Jaya area, Malaysia, University of Canterbury.
Santamouris, M. (2015). Analyzing the heat island magnitude and characteristics in one hundred Asian and Australian cities and regions. *Science of the Total Environment*, *512-513*, 582–598. https://doi.org/10.1016/j.scitotenv.2015.01.060
Sasaki, T., Wu, P., Mori, S., Hamada, J. I., Tauhid, Y. I., Yamanaka, M. D., … Kimura, F. (2004). Vertical moisture transport above the mixed layer around the mountains in western Sumatra. *Geophysical Research Letters*, *31*, L08106. https://doi.org/10.1029/2004GL019730
Sato, T., & Kimura, F. (2005). Diurnal cycle of convective instability around the Central Mountains in Japan during the warm season. *Journal of Atmospheric Sciences*, *62*(5), 1626–1636. https://doi.org/10.1175/JAS3423.1
Seasman, N. L., Ludwig, F. L., Donall, E. G., Warner, T. T., & Bhumralkar, C. M. (1988). Numerical studies of urban planetary boundary-layer structure under realistic synoptic conditions. *Journal of Applied Meteorology*, *28*, 760–781. https://doi.org/10.1175/1520-0450(1989)028
Sharma, A., Conry, P., Fernando, H. J. S., Hamlet, A. F., Hellmann, J. J., & Chen, F. (2016). Green and cool roofs to mitigate urban heat island effects in the Chicago metropolitan area: Evaluation with a regional climate model. *Environmental Research Letters*, *11*(6), 64,004. https://doi.org/10.1088/1748-9326/11/6/064004
Shin, H. H., & Hong, S.-Y. (2011). Intercomparison of planetary boundary-layer parametrizations in the WRF model for a single day from CASES-99. *Boundary-Layer Meteorology*, *139*(2), 261–281. https://doi.org/10.1007/s10546-010-9583-z
Skamarock, W. C., J. B. Klemp, D. O. Gill, D. M. Barker, M. G. Duda, W. Wang, & J. G. Powers (2008). A description of the Advanced Research WRF version 3, Boulder, Colorado, USA.
Sow, K. S., Juneng, L., Tangang, F. T., Hussin, A. G., & Mahmud, M. (2011). Numerical simulation of a severe late afternoon thunderstorm over Peninsular Malaysia. *Atmospheric Research*, *99*(2), 248–262. https://doi.org/10.1016/j.atmosres.2010.10.014
Storm, B., & Basu, S. (2010). The WRF model forecast-derived low-level wind shear climatology over the United States great plains. *Energies*, *3*(2), 258–276. https://doi.org/10.3390/en3020258
Stull, R. B. (1988). *An introduction to boundary layer meteorology* (Vol. 13, p. 666). Boston: Kluwer Academic. https://doi.org/10.1007/978-94-009-3027-8
Tangang, F. T., & Juneng, L. (2004). Mechanisms of Malaysian rainfall anomalies. *Journal of Climate*, *17*(18), 3616–3622. https://doi.org/10.1175/1520-0442(2004)017%3C3616:MOMRA%3E2.0.CO;2
Tangang, F. T., Juneng, L., Salimun, E., Kwan, M. S., Le Loh, J., & Muhammad, H. (2012). Climate change and variability over Malaysia: Gaps in science and research information. *Sains Malaysiana*, *41*(11), 1355–1366.
Teo, C., Koh, T., Chun-fung, J. L. O., & Chandra Bhatt, B. (2011). Principal component analysis of observed and modeled diurnal rainfall in the Maritime Continent. *Journal of Climate*, *24*(17), 4662–4675. https://doi.org/10.1175/2011JCLI4047.1
Thielen, J., Wobrock, W., Gadian, A., Mestayer, P. G., & Creutin, J. D. (2000). The possible influence of urban surfaces on rainfall development: A sensitivity study in 2D in the meso-??-scale. *Atmospheric Research*, *54*(1), 15–39. https://doi.org/10.1016/S0169-8095(00)00041-7
Thompson, W. T., Holt, T., & Pullen, J. (2007). Investigation of a sea breeze front in an urban environment. *Quarterly Journal of the Royal Meteorological Society*, *133*(624), 579–594. https://doi.org/10.1002/qj.52
Toth, Z. (2001). Ensemble forecasting in WRF. *Bulletin of the American Meteorological Society*, *82*(4), 695–697. https://doi.org/10.1175/1520-0477(2001)082%3C0695:MSEFIW%3E2.3.CO;2
Varikoden, H., Samah, A. A., & Babu, C. A. (2010). Spatial and temporal characteristics of rain intensity in the peninsular Malaysia using TRMM rain rate. *Journal of Hydrology*, *387*(3-4), 312–319. https://doi.org/10.1016/j.jhydrol.2010.04.023
von Glasow, R., Jickells, T. D., Liss, P. S., Mee, L., Raine, R., Ramachandran, P., … Zhu, T. (2013). Megacities and large urban agglomerations in the coastal zone: Interactions between atmosphere, land, and marine ecosystems. *Ambio*, *42*(1), 13–28. https://doi.org/10.1007/s13280-012-0343-9
Wang, B., Wu, R., & Lau, K.-M. (2001). Interannual variability of the Asian summer monsoon : Contrasts between the Indian and the Western North Pacific-East Asian Monsoons*. *Journal of Climate*, *14*(20), 4073–4090. https://doi.org/10.1175/1520-0442(2001)014%3C4073:IVOTAS%3E2.0.CO;2
Wang, W., Bruyère, C., Duda, M., Dudhia, J., Gill, D., Kavulich, M., … Fossell, K. (2015). *WRF-ARW V3.6.1: User's guide*, Boulder, Colorado, USA.
Xie, B., Fung, J. C. H., Chan, A., & Lau, A. (2012). Evaluation of nonlocal and local planetary boundary layer schemes in the WRF model. *Journal of Geophysical Research*, *117*, D12103. https://doi.org/10.1029/2011JD017080
Zhang, H., Pu, Z., & Zhang, X. (2013). Examination of errors in near-surface temperature and wind from WRF numerical simulations in regions of complex terrain. *Weather and Forecasting*, *28*(3), 893–914. https://doi.org/10.1175/WAF-D-12-00109.1
Zhang, N., Zhu, L., & Zhu, Y. (2011). Urban heat island and boundary layer structures under hot weather synoptic conditions: A case study of Suzhou City, China. *Advances in Atmospheric Sciences*, *28*(4), 855–865. https://doi.org/10.1007/s00376-010-0040-1
Zhong, S., & Yang, X. Q. (2015). Ensemble simulations of the urban effect on a summer rainfall event in the Great Beijing Metropolitan Area. *Atmospheric Research*, *153*(2015), 318–334. https://doi.org/10.1016/j.atmosres.2014.09.005